Migratory dermal γδ T cells determine the balance between lung immunity and tissue damage during *Nippostrongylus brasiliensis* infection

Pedro H. Papotto[1,✉], James E. Parkinson[1,2], Brian H.K. Chan[1,2], I-Hsuan Lin[3], Georgia E. Baldwin[1,2], Faith Denny[1], Lili Zhang[1,2], Rebecca J. Dodd[1,2], Stella T. Pearson[1], Natalie Fischhaber[1], Joanne E. Konkel[1], David R. Withers[4], Matthew R. Hepworth[1], and Judith E. Allen[1,2,✉]

[1]Lydia Becker Institute for Immunology & Infection, Faculty of Biology, Medicine & Health, Manchester Academic Health Science Centre, University of Manchester, Manchester, United Kingdom.
[2]Wellcome Centre for Cell-Matrix Research, Faculty of Biology, Medicine & Health, Manchester Academic Health Science Centre, University of Manchester, Manchester, United Kingdom.
[3]Bioinformatics Core Facility, Faculty of Biology Medicine and Health, University of Manchester, Manchester M13 9PT, United Kingdom.
[4]Institute of Immunology and Immunotherapy, College of Medical and Dental Sciences, University of Birmingham, Birmingham, United Kingdom.

Many helminth parasites migrate through multiple host organs during infection but how immunity is regulated across these tissues is still poorly understood. To investigate the cellular and molecular aspects of inter-tissue communication during infection we established a percutaneous infection model with the tissue-migrating nematode *Nippostrongylus brasiliensis*. High-dimension profiling of the initial cutaneous immune response revealed that dermal γδ T cells become activated, engage cell motility-associated transcriptional pathways and leave the skin after parasite invasion. Chemical and genetic inhibition of leukocyte migration prevents the accumulation of IL-17-producing γδ T cells in the lungs. Notably, bypassing the skin phase of infection, and therefore preventing dermal γδ T cell migration, dampens the increase in early IL-17 production in the lungs, and, instead, leads to enhanced IFN-γ responses together with increased lung damage. Collectively, our data highlights a critical skin–lung axis regulating host-parasite interactions and safeguarding lung health.

Correspondence:

pedro.papotto@manchester.ac.uk | judi.allen@manchester.ac.uk

Introduction

Complex multicellular organisms evolved to ensure that upon pathogen invasion each organ will respond appropriately to promote host survival(1). Achieving a balance that leads to pathogen elimination, whilst maintaining tissue integrity often requires the co-ordination of apparently opposing types of immune responses within particular tissues(2). Reaching this equilibrium is even more complex when we consider pathogens that migrate across different organs. As a result, our understanding of how immunity is orchestrated at the whole-organism level is still lacking.

Large multicellular parasites such as helminths are usually associated with type-2 immunity(3). Given the size of these pathogens and their (usually long) life cycles within the host, it is believed that the ultimate goal of type-2 immune responses is to prevent parasite migration through host tissues and to drive worm expulsion whilst keeping collateral damage to a minimum(4). Hence, type-2 immunity promotes different degrees of tissue remodelling(5), such as increased mucus production(6), smooth muscle contraction(7), extracellular matrix (ECM) changes(8), and fibrosis(9). The rodent parasite *Nippostrongylus brasiliensis* has been widely used to study the mechanisms regulating innate and adaptive type-2 immunity(10). The *N. brasiliensis* experimental model mimics key aspects of human hookworm infection, with larvae entering the host through the skin, and reaching the lung 18 to 48 hours post-infection (p.i.), where they moult before migrating to the small intestine(10). There, they become sexually mature and start releasing eggs before being expelled from the gut by 6 to 8 days p.i.(10). The importance of type-2 immunity in controlling *N. brasiliensis* infection is well-documented(3); in particular the IL-4/IL-13–IL-4Rα–Stat6 axis has been shown to be crucial for parasite expulsion and control of intestinal worm burden(3, 11). Surprisingly, work from our group has shown that in the lungs *N. brasiliensis* initially induces IL-17A production by γδ T cells, via Ym1 and IL-1β, which in turn is critical for the generation of subsequent type-2 immunity(12, 13). Paradoxically, IL-17A promotes neutrophil recruitment, contributing to increased tissue damage(14, 15) but also enhanced IL-33 release and, consequently, activation of ILC2s(14). In addition, IL-17A further enables a type-2-promoting environment by suppressing Interferon-γ (IFN-γ) production by γδ T cells and other innate-like lymphocytes(13), through mechanisms still not fully understood.

Despite early evidence of γδ T cell responses to helminth infections(16), the mechanisms behind their activation by these parasites are poorly defined. In contrast to conventional αβ $CD4^+$ and $CD8^+$ T cells, most murine γδ T cells acquire their effector functions during thymic development, reaching peripheral tissues readily capable of producing IL-17A or IFN-γ(17, 18). This functional dichotomy in murine γδ T cells is tightly linked to the variable γ (Vγ) chain of their T cell receptor (TCR)(18). Notably, the dermal layer of the skin exclusively harbours IL-17-producing γδ (γδ17) T cells, bearing Vγ4 and Vγ6 TCRs(18, 19). Dermal γδ T cells are a motile population that exhibits a slow but steady migration pattern to the skin-draining lymph nodes(19, 20). Whether these cells have the ability to migrate to other non-lymphoid organs during inflammation – akin to intestinal

PREPRINT

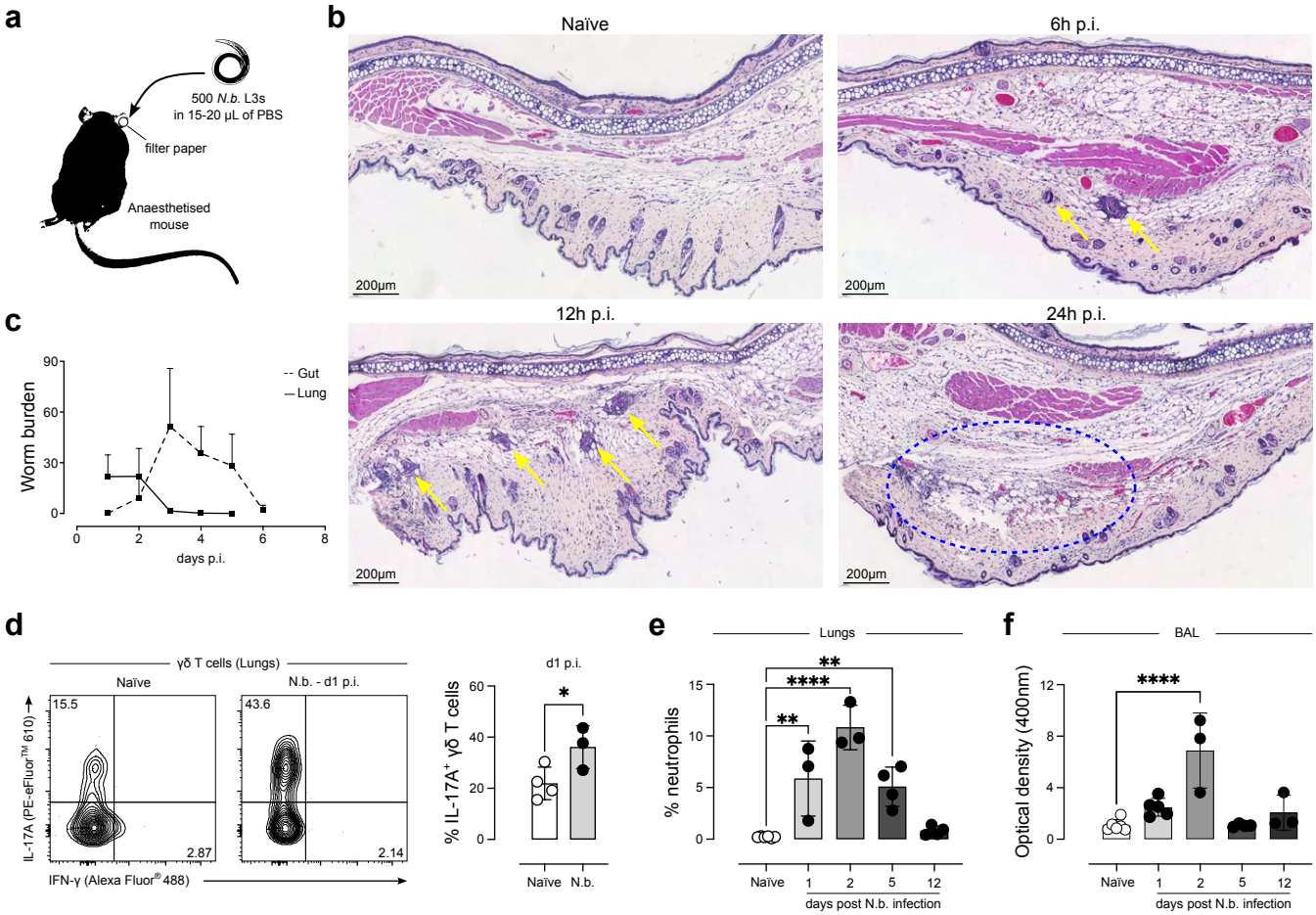

Fig. 1. *N. brasiliensis* p.c. infection recapitulates the hallmarks of the s.c. route of infection. a, Experimental procedure for *N. brasiliensis* p.c. infection. 500 L3s were added to a piece of filter paper and placed on the ear of an anaesthetised mouse for 30 minutes. **b**, Representative H&E staining micrography of ear sections from naïve (top left) and *N.brasiliensis*-infected C57BL/6J mice at 6h (top right), 12h (bottom left) and 24h p.i. (bottom right); yellow arrows indicate *N. brasiliensis* larvae, and the blue circle shows an inflammatory focus. **c**, Worm burden measured in the lungs (dashed line) and small intestines (full line) throughout the course of *N. brasiliensis* p.c. infection. **d**, Flow cytometry analysis of intracellular IL-17A and IFN-γ in γδ T cells isolated from the lungs of naïve and *N.brasiliensis*-infected C57BL/6J mice and stimulated *ex vivo* for 4h. Summary graph showing the percentages of IL-17A$^+$ cells within the γδ T cell population (n = 3-4 mice per group; representative of at least 3 independent experiments). **e**, Frequencies of neutrophils within total leukocytes in the BAL throughout the course of *N. brasiliensis* p.c. infection (n = 3-6 mice per group). **f**, Optical density of the BAL of naïve and *N.brasiliensis*-infected C57BL/6J mice measured at 400nm to quantify lung bleeding (n = 3-6 mice per group). **c-f**, Error bars represent mean±SD. Normality of the samples was assessed with Shapiro-Wilk normality test; statistical analysis was then performed using Student's t test (**d**) or one-way ANOVA test (**e, f**). * $p < 0.05$; ** $p < 0.01$; **** $p < 0.0001$

γδ17 T cells(21, 22) – is yet to be determined. Thus, we hypothesised that activation of skin γδ T cells by N. brasiliensis may have consequences beyond their tissue of residency, potentially setting the tone for the subsequent lung immunity to the parasite.

Here we optimised a percutaneous (p.c.) *N. brasiliensis* infection model mimicking the natural steps of parasite invasion and migration through the skin. This allowed us to generate a comprehensive analysis of the early immune events taking place in the skin from 6 to 24 hours after larval invasion. *N. brasiliensis* larvae induced the recruitment of neutrophils and monocytes to the skin, but in contrast to the lungs, did not induce an increase in IL-17 production by γδ T cells. Instead, dermal γδ T cells upregulated pathways related to cell migration and travelled to the lungs, where they were responsible for the increase in γδ17 T cells and suppression of IFN-γ production. Finally, bypassing the skin phase of the infection through intravenous (i.v.) injection of *N. brasiliensis* larvae, prevented dermal γδ17 T cell migration, and subsequently induced the expansion of lung IFN-γ producing γδ (γδ1) T cells and increased tissue damage.

Results

Percutaneous N. brasiliensis *infection recapitulates the major hallmarks of the subcutaneous injection model*

Standard laboratory practice of inducing *N. brasiliensis* infection involves subcutaneous (s.c.) injection of larvae. While practical, it fails to recapitulate natural events in the skin that may determine subsequent events in the lungs. We thus needed a model that elicits immune responses along all the strata of the skin and avoids needle-induced effects, but also generates a consistent and reproducible infection in the lung and gut. To achieve this, we adapted a protocol from the 1970s(23) and placed a moist filter paper containing 500 *N. brasiliensis* L3s on the ears of anaesthetised mice for 30 minutes (**Fig. 1a**). This protocol ensures larvae penetrate through the skin, where the parasites could be found, near

the base of the ear, up until 12h p.i. (**Fig. 1b**); at 24h p.i. tissue damage was evident, but larvae were no longer found in the skin (**Fig. 1b**). NanoString analysis of whole-skin tissue (**Extended Data Fig. 1a**) indicated that transcriptional changes were evident by 6h p.i., with the biggest differences observed at 24h p.i. (**Extended Data Fig. 1b**). Pathway analysis showed that differentially upregulated genes at 24h p.i. related to cytokine signalling, response to LPS and type-I IFN production, supporting published findings using non-viable parasites injected intradermally(24, 25) (**Extended Data Fig. 1c**). Differentially downregulated genes, on the other hand, were mostly associated with pathways regulating cell-cell adhesion (**Extended Data Fig. 1d**). Importantly, the p.c. route led to infection kinetics akin to the s.c. model (**Extended Data Fig. 1e**) with the parasite being found in the lungs between days 1 and 2 p.i., then in the intestines between days 2 and 5 p.i., being mostly cleared after day 6 p.i. (**Fig. 1c**). Critical for this study, *N. brasiliensis* p.c. infection induced an increase in lung γδ17 T cells at day 1 p.i (**Fig. 1d**), corroborating published data using s.c. infection(12, 13). As a result, we found neutrophil levels to be increased in the bronchoalveolar lavage (BAL) as early as day 1 p.i., remaining elevated until day 5 p.i., and returning to naïve levels at day 12 p.i. (**Fig. 1e**). Lung damage was characterised by evidence of haemorrhage in the BAL, which followed the pattern of neutrophil kinetics, being more evident at the peak of BAL neutrophilia (**Fig. 1f**), mirroring the findings from the s.c. model(26) (**Extended Data Fig. 1f, g**). Type-2 immunity also followed the kinetics of s.c. infections, with p.c.-infected mice showing an increase in IL-5$^+$ ILC2s as early as day 1 p.i., and IL-13$^+$ ILC2s from days 5 to 12(27) (**Extended Data Fig. 1h**). We found that IL-5 (**Extended Data Fig. 1i**) and IL-13 (**Extended Data Fig. 1j**) production by CD4$^+$ T cells peaked at day 12 p.i., with eosinophil recruitment following the same pattern (**Extended Data Fig. 1k**). Overall, our p.c. *N. brasiliensis* infection model recapitulates the major hallmarks of the pulmonary response against migrating larvae, making it a useful tool in the study of skin – lung communication.

Bypass of the skin phase of infection induces increased IFN-γ production and lung haemorrhage

In order to evaluate the role of the skin phase of the infection in regulating lung immunity, we compared p.c.-infected mice with animals that were infected intravenously (i.v.) with *N. brasiliensis* larvae (**Fig. 2a**). On a tissue-wide level, NanoString analysis indicated that p.c. and i.v. infections induce distinct transcriptional changes in the lungs (**Fig. 2b**), with p.c.-infected mice showing increased expression of genes related to neutrophil recruitment (such as *Sele* and *Cxcl2*) and their i.v. counterparts exhibiting an increase in the expression of MHC-related genes (e.g., *Cd74*, *Tap1*, *H2-DMb2*, *H2-Ab1*, *H2-Eb1* and *H2-Ob*) and type-1 effector genes, such as *Ccl5* and *Klrk1* (**Fig. 2c**). Of note, these discrete transcriptional changes are not due to differences in infection efficacy, as the two routes of infection led to a comparable worm burden in the lungs at days 1 and 2 p.i. (**Extended Data Fig. 2a**). As expected from the previous flow cytometry data (**Fig. 1d**), *N. brasiliensis* p.c.-infected mice showed an enrichment in pathways related to IL-17 signalling (**Fig. 2d**), which was something not observed in i.v.-infected animals that in turn displayed an enrichment in pathways related to wound healing (**Fig. 2e**). Accordingly, *N. brasiliensis* i.v. infections did not induce an increase in lung γδ17 T cells, in contrast to what we observed in p.c. infections (**Fig. 2f**). Interestingly, i.v.-infected mice showed, instead, an increase in the frequency of IFN-γ-producing γδ (γδ1) T cells in the lungs when compared to naïve and p.c.-infected animals (**Fig. 2f**). In addition, *N. brasiliensis* i.v. infection led to enhanced type-2 cytokine production, with increased levels of IL-13, IL-9 and IL-5 (**Extended Data Fig. 2b**). As expected from their failure to induce γδ17 T cell responses, i.v.-infected mice also failed to recruit neutrophils to the lungs (**Fig. 2g**). To our surprise, however, despite not inducing a neutrophilic response in the lungs, bypass of the skin resulted in increased lung haemorrhage (**Fig. 2h and Extended Data Fig. 2c**). An increase of neutrophils, eosinophils, T cells and B cells was observed in the BAL of i.v.-infected mice but not in p.c.-infected mice (**Extended Data Fig. 2d**), possibly reflecting the differential haemorrhagic responses in these mice (**Fig 2h**). As IFN-γ has been shown to mediate vascular integrity and lung bleeding during viral infection(28), we infected *Ifngr*$^{-/-}$ mice and their *Ifngr*$^{+/+}$ littermates with *N. brasiliensis* i.v. (**Fig. 2i**). Interestingly, *Ifngr*$^{-/-}$ mice presented a decrease in lung haemorrhage, when compared to wild-type (WT) controls (**Fig. 2j and Extended Fig. 2e**). Thus, our results indicate that bypassing the skin phase of *N. brasiliensis* infection fails to induce an increase in γδ17 T cells or associated neutrophil recruitment, and instead induces IFN-γ production by γδ T cells with increased lung bleeding.

Next, to better understand the initial immune response of lung γδ T cells to migrating *N. brasiliensis* larvae, at day 1 p.i. we sorted all the major lung populations of innate lymphocytes in p.c.- and i.v.-infected mice and performed single-cell RNA sequencing (scRNAseq) analysis (**Fig. 3a**). We identified and annotated 16 distinct cell subsets across all treatment groups (**Fig. 3b**). *N. brasiliensis* p.c. and i.v. infections led to discrete changes in the immune populations analysed when compared to naïve mice (**Fig. 3c**). Relative frequencies of γδ T cell populations confirmed our flow cytometry data, with a marked decrease in naïve and γδ1 T cells in p.c.-infected mice, juxtaposed by an increase in γδ1 T cells observed during i.v. infection (**Fig. 3d**). Moreover, across different populations of IFN-γ-producing cells (with the exception of ILC1), p.c. infection led to a decrease in the expression of a type-1 effector gene module (**Extended Data Table 1**), when compared to their i.v.-infected counterparts and naïve controls (**Fig. 3e**). Conversely, all IFN-γ-producing populations from i.v.-infected mice displayed an activation of the same type-1 effector gene module (**Fig. 3e**). With regards to IL-17-producing cells, *N. brasiliensis* p.c. infection induced an increase in the relative frequencies of Vγ6$^+$ and Vγ6$^-$ γδ17 T cells (**Fig. 3d**), whereas i.v. infec-

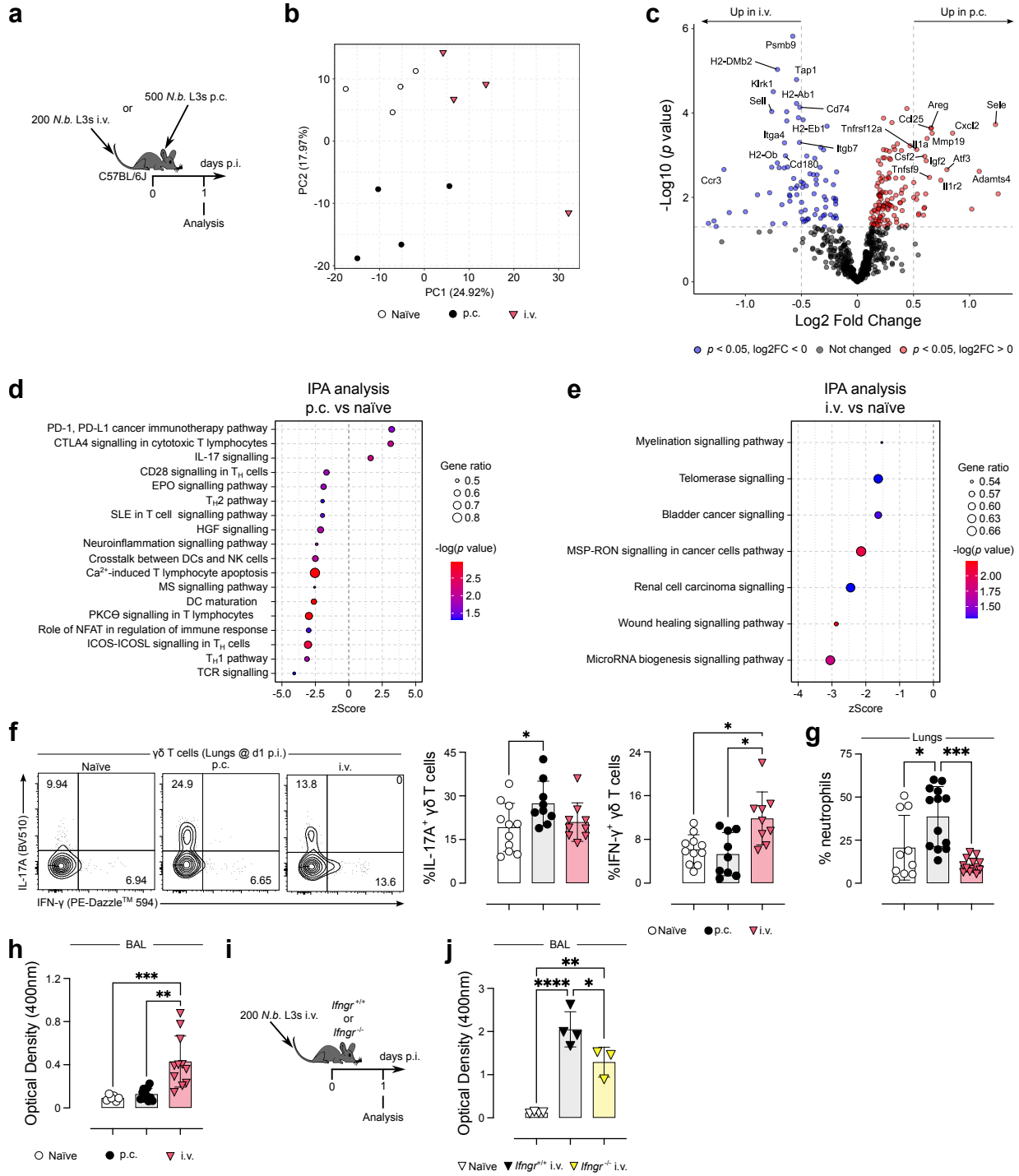

Fig. 2. Bypassing the skin phase of infection precludes the induction of lung type-17 responses and results in increased IFN-γ-dependent lung bleeding during *N. brasiliensis* larvae migration. **a**, Experimental approach used for *N. brasiliensis* p.c. and i.v. infections. For the p.c. route, mice were infected with 500 L3s as described in Fig. 1a; for the i.v. route, mice were injected with 200 L3s in sterile PBS. **b**, Total lung RNA from naïve (white circles), p.c.- (black circles) and i.v.-infected (pink triangles) C57BL/6J mice was analysed with the Mouse Myeloid Innate Immunity V2 NanoString panel and total sample variation was summarised via principal component analysis (PCA) across all genes. (n = 4 mice per group) **c**, Differentially expressed genes (DEGs) were visualised using a volcano plot, genes significantly upregulated in p.c. infection (red) and i.v. (blue) where characterised by having a *p* value of <0.05. d, e, Overrepresented pathways determined via Ingenuity Pathway Analysis (IPA) in DEGs from p.c.-infected vs naïve controls (**d**) and i.v.-infected vs naïve controls (**e**). **f**, Flow cytometry analysis of intracellular IL-17A and IFN-γ in γδ T cells isolated from the lungs of naïve (white circles), p.c. (black circles) and i.v. (pink triangles) *N. brasiliensis*-infected C57BL/6J mice and stimulated *ex vivo* for 4h. Summary graph showing the percentages of IL-17A$^+$ and IFN-γ$^+$ cells within the γδ T cell population (n = 9-11 mice per group; pool of 2 independent experiments). **g**, Frequencies of neutrophils within total leukocytes in the lungs of naïve (white circles), p.c. (black circles) and i.v. (pink triangles) *N. brasiliensis*-infected C57BL/6J mice (n = 10-14 mice per group; pool of 3 independent experiments). **h**, Optical density of the BAL of naïve (white circles), p.c. (black circles) and i.v. (pink triangles) *N. brasiliensis*-infected C57BL/6J mice measured at 400nm to quantify bleeding into the airways. (n = 6-11 mice per group; pool of 2 independent experiments). **i**, *Ifngr*$^{-/-}$ and their WT counterparts were infected with 200 *N. brasiliensis* L3s i.v. **j**, Optical density of the BAL of naïve (white triangles), and *N.brasiliensis*-infected *Ifngr*$^{+/+}$ (black triangles) and *Ifngr*$^{-/-}$ (yellow triangles) mice measured at 400nm to quantify bleeding into the airways. (n = 3-4 mice per group). **f-j**, Error bars represent mean±SD. Normality of the samples was assessed with Shapiro-Wilk normality test; statistical analysis was then performed using Kruskal-Wallis or one-way ANOVA test (**e, f**). * $p < 0.05$; ** $p < 0.01$; *** $p < 0.001$; **** $p < 0.0001$

tions led to a specific decrease in Vγ6$^+$ γδ17 T cells (**Fig. 3d**). Furthermore, relative to naïve mice, Vγ6$^+$ and Vγ6$^-$ γδ17 T cells from i.v.-infected animals displayed only 3 and 1 differentially expressed genes (DEGs) respectively (**Fig. 3f, g**), whereas p.c. infection led to 44 DEGs in Vγ6$^+$ γδ17 T cells (**Fig. 3f, h**) and 29 DEGs in Vγ6$^-$ γδ17 T cells (**Fig. 3g and Extended Data Fig. 3a**). Interestingly, we found upregulated DEGs from p.c. Vγ6$^+$ γδ17 T cells to be associated with pathways related to T cell activation (**Fig. 3i**); downregulated DEGs, on the other hand, were associated with positive regulation of cell–substrate adhesion (**Fig. 3j**). Taken together, our results indicate that activation of γδ17 T cells in the lungs during *N. brasiliensis* infection only happens when the larvae migrate through the skin, which also induces the suppression of IFN-γ-producing cells. In addition, bypassing the skin phase of the infection leads to an enrichment in lung type-1 cells and an increase in IFN-γ-biased transcriptional signatures.

N. brasiliensis *induces skin type-2 immune responses and the activation of migratory pathways in dermal γδ T cells*

As some of the enriched pathways in the Vγ6$^+$ γδ17 T cells from the lungs of p.c.-infected mice suggested decreased ECM adhesion, and therefore increased motility, we hypothesised that these cells were being activated elsewhere. Hence, we next dissected the effect of invading larvae on the cellular immune responses taking place in the skin, in particular by γδ T cells (**Fig. 4a**). In notable contrast to what we observed in the lungs, intracellular staining of skin cells stimulated *ex vivo* showed no differences in IL-17A$^+$ and IL-17F$^+$ dermal γδ T cells between naïve and *N. brasiliensis*-infected mice (**Fig. 4b**). Likewise, at 6h p.i. *N. brasiliensis* infection did not induce an increase of IL-17A and/or IL-17F in skin tissue lysates (**Extended Data Fig. 4a**). Instead, *N. brasiliensis* larvae induced an increase in the skin levels of IL-6 and type-2 cytokines such as TSLP, IL-33, IL-5 and Ym1 (**Extended Data Fig. 4a, b**). Despite the lack of differences in the production of IL-17 cytokines, infected mice displayed an increase in neutrophils (but not in monocytes) in the skin already at 6h p.i., being found mainly around *N. brasiliensis* larvae (**Extended Data Fig. 4c**). At 24h p.i., infected mice showed marked changes in the immune cell populations present in the skin (**Fig. 4c and Extended Data Fig. 4d**), with monocytes and neutrophils being the only two populations increased upon infection (**Fig. 4c and Extended Data Fig. 4d**), as previously described(32). Interestingly, dermal γδ T cells were found to be decreased in infected mice (**Fig. 4c**).

At this point, while *N. brasiliensis* infection increases γδ17 T cells in the lungs, and in the skin, not only is IL-17 production by dermal γδ T cells unchanged but cell numbers decrease upon infection. Therefore, we considered the possibility of dermal γδ T cells leaving the tissue upon encountering the invading larvae. In order to investigate the effects of *N. brasiliensis* larvae on skin γδ T cells, we sorted both dendritic epidermal T cells (DETCs) and dermal γδ T cells from naïve and *N. brasiliensis*-infected mice at 6h p.i. for subsequent RNA sequencing (**Fig. 4d**). Even within the short timeframe selected, *N. brasiliensis* infection induced significant changes in the transcriptional profile of dermal γδ T cells (**Fig. 4e**), with almost 200 differentially expressed genes (DEGs) between naïve and infected mice (**Fig. 4f and Extended Data Table 2**). Notably, most canonical γδ17 T cell activation genes, such as *Rorc*, *Il17a*, *Il23r*, *Gpr183* and *Blk*, were not significantly different between dermal γδ T cells from naïve and infected mice (**Fig. 4f and Extended Data Table 2**), corroborating our protein data (**Fig. 4b and Extended Data Fig. 4a**) and suggesting the involvement of other signalling pathways. In fact, DEGs from dermal γδ T cells in *N. brasiliensis*-infected mice were found to be involved mostly with cell membrane and ECM components (**Fig. 4g**). Accordingly, we found pathways related to cell migration (regulated by genes such as *Sparc*, *Dcn* and *Cd63*) and catabolic processes (mediated by genes such as *Il6*, *Fastkd2* and *Dkc1*) to be enriched in upregulated DEGs (**Fig. 4h**). Downregulated DEGs were found to be mainly associated with the regulation of cytotoxic pathways (e.g., *Nkg7*, *Prf1* and *Havcr2*) and cell-cell adhesion (e.g., *Tjp1*, *Cdh1* and *Cd160*; **Fig. 4i**). Hence, upon *N. brasiliensis* infection dermal γδ T cells engage a transcriptional programme directed to cell migration. Indeed, dermal γδ T cells from infected mice showed increased gene expression of the S1P receptors *S1pr1* and *S1pr4*, and the chemokine receptor *Ccr2*, all of which have been shown to regulate γδ17 T cell migration during inflammation(33, 34) (**Fig. 4j**). Importantly, these changes seem to be restricted to dermal γδ T cells, as DETCs from *N. brasiliensis*-infected mice showed no relevant transcriptional differences when compared to their naïve counterparts (**Extended Data Fig. 4e**). Collectively, our analysis of the early immune events in the skin of *N. brasiliensis*-infected mice showed an increase in type-2 cytokines and neutrophils, but not in the production of IL-17A or IL-17F by γδ T cells, as expected. Instead, during larvae invasion dermal γδ T cells appear to get activated and engage a migratory programme, leading to their disappearance from the skin after 24h p.i.

Dermal γδ T cells migrate to the lungs early during N. brasiliensis *infection*

Our data implied that the increase in γδ17 T cells in the lungs during *N. brasiliensis* infection could stem from the migration of dermal γδ T cells and not local expansion – as Ki67 staining showed no differences in the proliferation status of lung γδ17 T cells between naïve and *N. brasiliensis*-infected mice at day 1 p.i. (**Extended Data Fig. 5a**). In order to track migratory γδ T cells, we employed an inducible *Id2*^{CreERT2}x*Rosa26*^{RFP} reporter mouse line in which, by treating mice topically with 4-hydroxytamoxifen (4OH-T) on the skin area where the *N. brasiliensis* infection would later take place (**Fig. 5a**), we achieved a sizeable proportion of innate-like lymphocytes – including dermal γδ T cells – expressing the red fluorescent protein RFP (**Fig. 5b and Extended Data Fig. 5b**). The expected increase in IL-17A$^+$ IL-17F$^-$ and IL-17A$^+$IL-17F$^+$ γδ T cells was observed in the

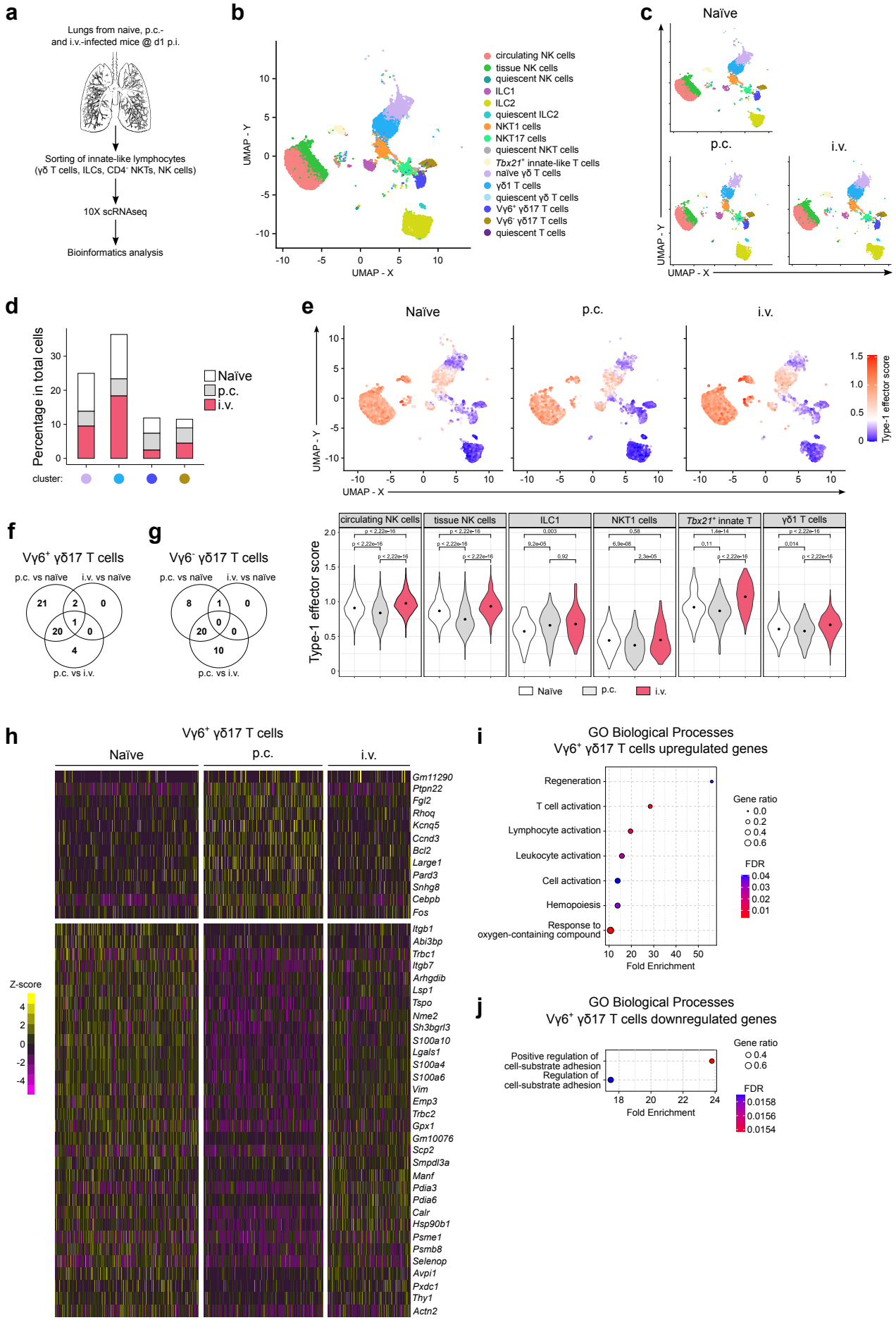
a
Lungs from naive, p.c.- and i.v.-infected mice @ d1 p.i.
Sorting of innate-like lymphocytes (γδ T cells, ILCs, CD4⁻ NKTs, NK cells)
10X scRNAseq
Bioinformatics analysis
b
UMAP - Y
UMAP - X
circulating NK cells
tissue NK cells
quiescent NK cells
ILC1
ILC2
quiescent ILC2
NKT1 cells
NKT17 cells
quiescent NKT cells
Tbx21⁺ innate-like T cells
naïve γδ T cells
γδ1 T cells
quiescent γδ T cells
Vγ6⁺ γδ17 T cells
Vγ6⁻ γδ17 T cells
quiescent T cells
c
Naïve
p.c.
i.v.
UMAP - Y
UMAP - X
d
Percentage in total cells
Naïve
p.c.
i.v.
cluster:
e
Naïve
p.c.
i.v.
UMAP - Y
UMAP - X
Type-1 effector score
f
Vγ6⁺ γδ17 T cells
p.c. vs naïve
i.v. vs naïve
p.c. vs i.v.
21
2
0
1
20
0
4
g
Vγ6⁻ γδ17 T cells
p.c. vs naïve
i.v. vs naïve
p.c. vs i.v.
8
1
0
0
20
0
10
circulating NK cells
tissue NK cells
ILC1
NKT1 cells
Tbx21⁺ innate T
γδ1 T cells
Type-1 effector score
Naïve
p.c.
i.v.
h
Vγ6⁺ γδ17 T cells
Naïve
p.c.
i.v.
Gm11290
Ptpn22
Fgl2
Rhoq
Kcnq5
Ccnd3
Bcl2
Large1
Pard3
Snhg8
Cebpb
Fos
Itgb1
Abi3bp
Trbc1
Itgb7
Arhgdib
Lsp1
Tspo
Nme2
Sh3bgrl3
S100a10
Lgals1
S100a4
S100a6
Vim
Emp3
Trbc2
Gpx1
Gm10076
Scp2
Smpdl3a
Manf
Pdia3
Pdia6
Calr
Hsp90b1
Psme1
Psmb8
Selenop
Avpi1
Pxdc1
Thy1
Actn2
Z-score
i
GO Biological Processes
Vγ6⁺ γδ17 T cells upregulated genes
Regeneration
T cell activation
Lymphocyte activation
Leukocyte activation
Cell activation
Hemopoiesis
Response to oxygen-containing compound
Fold Enrichment
Gene ratio
FDR
j
GO Biological Processes
Vγ6⁺ γδ17 T cells downregulated genes
Positive regulation of cell-substrate adhesion
Regulation of cell-substrate adhesion
Fold Enrichment
Gene ratio
FDR

Fig. 3 *(previous page)*. P.c., but not i.v., *N. brasiliensis* infection induces the activation of Vγ6⁺ γδ17 T cells and suppression of IFN-γ-producing innate lymphocytes. **a**, Schematic showing the strategy used for sorting innate lymphocytes prior to scRNAseq. **b,c**, Manually annotated Louvain clusters projected onto two dimensional UMAP plot (**b**) and separated by infection status (**c**). **d**, Percentage of total cell barcodes within different infection groups for naïve γδ T cells (lilac circle), γδ1 T cells (light blue circle), Vγ6⁺ γδ17 T cells (dark blue circle), Vγ6⁻ γδ17 T cells (golden circle) clusters. **e**, Type-1 effector signature was generated from a list of manually curated genes available from the literature(29–31) and calculated average standard scores (z-score) of this gene module were used to colour cells projected on a UMAP plot (red = high, blue = low). Summary violin plots showing the per-cell Type-1 effector score across different cell clusters and treatment conditions (Naïve = white; p.c. = grey; i.v. = pink). **f, g**, Venn diagram showing the overlap of DEGs (defined as adjusted *p* value <0.05, absolute log2 fold change of >1 and mean expression value >1) between different infection route comparisons for Vγ6⁺ (**f**) and Vγ6⁻ γδ17 T cells (**g**). **h**, Heatmap showing the DEGs in Vγ6⁺ γδ17 T cells from naïve, p.c.- and i.v.-infected animals. Scale represents scaled and centred z-scores. **i,j**, Overrepresented GO: biological processes in upregulated (**i**) and downregulated (**j**) genes in Vγ6⁺ γδ17 T cells from p.c.-infected animals. **b-j**, scRNAseq data consists of sorted cells pooled from 4 mice per group.

lungs of *Id2*$^{\text{CreERT2}}$x*Rosa26*^{RFP} mice upon *N. brasiliensis* infection (**Fig. 5c**). We observed a trend for increased RFP representation within total lung γδ T cells ($p = 0.0592$; **Fig. 5d**), which was mostly driven by the accumulation of RFP⁺ cells within the population of Vγ6, and not Vγ4⁺ or Vγ1⁺, γδ T cells ($p = 0.0592$; **Extended Data Fig. 5c**). Critically, we found an increased proportion of RFP⁺ cells within IL-17A⁺IL17F⁺ γδ T cells from *N. brasiliensis*-infected mice when compared to naïve controls (**Fig. 5e**), corroborating our hypothesis that, in this model, activated γδ17 T cells in the lungs originate from the skin. Of note, *N. brasiliensis* infection did not induce an increase in RFP⁺ γδ T cells in the ear draining lymph nodes at the timepoint analysed (**Extended Data Fig. 5d**). As an alternative approach, we employed *Trdc*$^{\text{CreERT2}}$x*Rosa26*^{RFP} reporter mice using a similar protocol as described above (**Extended Data Fig. 5e**) to specifically track skin γδ T cells. Despite lower Cre recombinase penetrance in these mice (**Extended Data Fig. 5f**), we observed a smaller, but significant, increase in RFP⁺ γδ T cells in the lungs of *N. brasiliensis*-infected mice compared to controls (**Extended Data Fig. 5g**). Thus, our results suggest that skin-derived γδ T cells migrate to the lungs early during *N. brasiliensis* infection and are responsible for the increase in IL-17 production in the lungs. To further confirm a role for dermal γδ17 T cells in the establishment of lung type-17 immune responses early during *N. brasiliensis* larvae migration, we used *Id2*$^{\text{CreERT2}}$ mice crossed with *Rorc*^{fl} animals to deplete IL-17-producing innate lymphocytes (*Rorc*$^{\Delta Id2}$; **Extended Data Fig. 5h**); topical treatment with 4OH-T ensured site-specific Cre activity (**Fig. 5f**). Upon *N. brasiliensis* infection, *Rorc*$^{\Delta Id2}$ mice failed to induce either an increase in lung γδ17 T cells or the suppression of γδ1 T cells (**Fig. 5g**).

Finally, to gain insight into the mechanisms underlying dermal γδ17 T cell migration, we prevented cell trafficking by employing transgenic mouse models and small molecule inhibitors. γδ T cell migration has been shown to be dependent on S1PR(33), and we observed an increased expression of *S1pr1* and *S1pr4* in dermal γδ T cells upon *N. brasiliensis* infection (**Fig. 4j**). Therefore, we blocked leukocyte trafficking by using the S1PR modulator FTY720 in our experimental model (**Extended Data Fig. 5i**). FTY720-treated mice did not display either the expected increase in lung γδ17 T cells or the parallel suppression of IFN-γ (**Extended Data Fig. 5j**) nor did they exhibit significant changes in Vγ usage upon *N. brasiliensis* infection (**Extended Data Fig. 5k**). CCR2 has also been shown to mediate γδ T cell migration during inflammation(34), and we observed an increase in its gene expression in dermal γδ T cells upon *N. brasiliensis* infection (**Fig 4j**). Thus, we infected *Ccr2*$^{-/-}$ mice and their WT littermates with *N. brasiliensis* and analysed their lung immune responses (**Fig. 5h**). As expected, infected WT mice displayed an increase in γδ17 T cells in the lungs together with a decrease in IFN-γ-producing γδ T cells, as expected (**Fig. 5i**). Infected *Ccr2*$^{-/-}$ mice, on the other hand, showed differences in neither lung γδ17 T cells, nor γδ1 T cells (**Fig. 5j**). *N. brasiliensis* infection also induced a shift in Vγ usage in WT lung γδ T cells, with a marked increase in Vγ6 cells but not in *Ccr2*$^{-/-}$ mice (**Fig. 5k and Extended Data Fig. 5l, m**). Altogether, our results reveal that dermal Vγ6 γδ17 T cells migrate from the skin to the lungs, in a CCR2- and S1PR-dependent manner, early during *N. brasiliensis* infection to kickstart an IL-17-mediated immune response and prevent IFN-γ-mediated tissue damage.

Discussion

Tissue-migrating parasites constitute unique models for investigating the molecular cues underlying inter-tissue communication. Whereas pathogen type has traditionally been regarded as the driver of different types of immune responses, the tissue where the host-pathogen encounter occurs has also been proposed to play a big part in this process(35). Here we show that during experimental *N. brasiliensis* infection, dermal γδ17 T cells are activated in the skin and then migrate to the lungs, in a CCR2- and S1PR-dependent fashion, during the early stages of the parasite life cycle within the host. There, these cells orchestrate the initial events that shape the pulmonary immune response against *N. brasiliensis*: production of IL-17 and suppression of IFN-γ-producing cells. Bypassing the skin phase of infection precludes the migration of γδ17 T cells from the skin to the lungs, leading to marked changes in the pulmonary immune response to *N. brasiliensis*, culminating in an initial response in the lung akin to the one observed in the skin. Importantly, γδ17 T cells are not activated in loco by *N. brasiliensis* larvae arriving directly to the lungs; instead, i.v. infections induce the activation of IFN-γ-producing innate lymphocytes and increase tissue damage.

Using the *N. brasiliensis* infection model, we found that the same pathogen induces similar responses in both the skin and lungs, but only when the skin phase is bypassed. Despite both being barrier tissues, skin and lung possess obvious structural and functional differences in addition to discrete resident immune cell populations, arguing that pathogen-derived pathogen-associated molecular patterns (PAMPs) override tissue particularities in setting up the

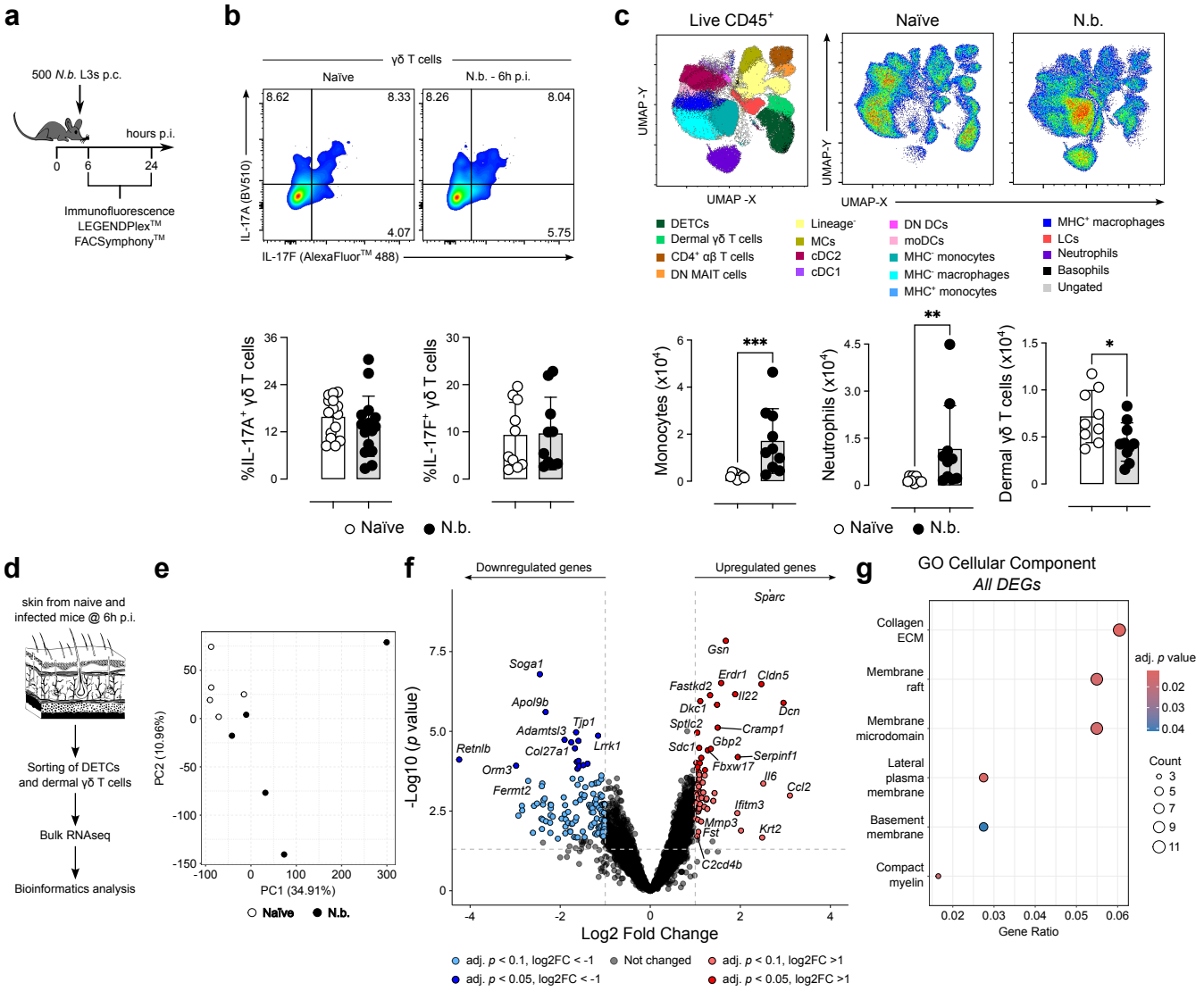
a
500 N.b. L3s p.c.
hours p.i.
0
6
24
Immunofluorescence
LEGENDPlex™
FACSymphony™
b
γδ T cells
Naïve
N.b. - 6h p.i.
8.62
8.33
4.07
8.26
8.04
5.75
IL-17A (BV510)
IL-17F (AlexaFluor™ 488)
%IL-17A+ γδ T cells
%IL-17F+ γδ T cells
Naïve
N.b.
c
Live CD45+
Naïve
N.b.
UMAP -Y
UMAP -X
DETCs
Dermal γδ T cells
CD4+ αβ T cells
DN MAIT cells
Lineage-
MCs
cDC2
cDC1
DN DCs
moDCs
MHC- monocytes
MHC- macrophages
MHC+ monocytes
MHC+ macrophages
LCs
Neutrophils
Basophils
Ungated
Monocytes (x10^4)
Neutrophils (x10^4)
Dermal γδ T cells (x10^4)
***
**
*
Naïve
N.b.
d
skin from naive and infected mice @ 6h p.i.
Sorting of DETCs and dermal γδ T cells
Bulk RNAseq
Bioinformatics analysis
e
PC2 (10.96%)
PC1 (34.91%)
Naïve
N.b.
f
Downregulated genes
Upregulated genes
-Log10 (p value)
Log2 Fold Change
Sparc
Gsn
Soga1
Erdr1
Cldn5
Fastkd2
Il22
Apol9b
Dkc1
Dcn
Tjp1
Sptlc2
Cramp1
Adamtsl3
Gbp2
Retnlb
Col27a1
Lrrk1
Sdc1
Serpinf1
Orm3
Fbxw17
Il6
Fermt2
Ccl2
Ifitm3
Mmp3
Krt2
Fst
C2cd4b
adj. p < 0.1, log2FC < -1
Not changed
adj. p < 0.1, log2FC >1
adj. p < 0.05, log2FC < -1
adj. p < 0.05, log2FC >1
g
GO Cellular Component
All DEGs
Collagen ECM
Membrane raft
Membrane microdomain
Lateral plasma membrane
Basement membrane
Compact myelin
adj. p value
Count
Gene Ratio
h
GO Biological Process
Upregulated genes
Cellular nitrogen compound catabolic process
Heterocycle catabolic process
Aromatic compound catabolic process
Organic cyclic compound catabolic process
Epithelial cell migration
Epithelium migration
Tissue migration
Negative regulation of angiogenesis
Negative regulation of blood vessel morphogenesis
Negative regulation of vasculature development
adj. p value
Count
Gene Ratio
i
GO Biological Process
Downregulated genes
Regulation of inflammatory response
Positive relation of cell-cell adhesion
Immune response to tumour cell
Response to tumour cell
Regulation of K+ transmembrane transport
Exocrine system development
Regulation of NK cell activation
Regulation of branching in salivary gland morphogenesis
NK cell mediated immune response to tumour cell
Granzime-mediated programmed cell death siganlling pathway
adj. p value
Count
Gene Ratio
j
S1P receptors
Chemokine receptors
Other
S1pr1
S1pr2
S1pr4
Ccr2
Ccrl2
Ccr4
Ccr5
Ccr6
Ccr7
Ccr8
Ccr9
Selplg
Itgae
Expression (Z-Score)
Naïve
N.b.

Fig. 4 *(previous page). N. brasiliensis* larvae induce a migratory transcriptional program in dermal γδ T cells. **a**, C57BL/6J mice were infected with 500 *N. brasiliensis* L3s p.c. and analysed at 6h and 24h p.i. **b**, Flow cytometry analysis of intracellular IL-17A and IL-17F in dermal γδ T cells isolated from the skin of naïve (white circles) and *N. brasiliensis*-infected (black circles) mice and stimulated *ex vivo* for 3h. Summary graph showing the percentages of IL-17A$^+$ and IL-17F$^+$ cells within the γδ T cell population (n = 10-15 mice per group; pool of 3 independent experiments for IL-17A and pool of 2 independent experiments for IL-17F). **c**, Representative UMAP plot (pool of 5 mice per group) summarising the flow cytometry analysis of skin immune cell populations (left) and density UMAP plots summarising the data for naïve (middle) and *N. brasiliensis*-infected (right) mice. Summary graph showing the numbers of skin monocytes, neutrophils and dermal γδ T cells (n = 9-10 mice per group; pool of 2 independent experiments). **d**, Experimental approach employed to obtain the transcriptional signature of DETCs and dermal γδ T cells from naïve and *N. brasiliensis*-infected C57BL/6J mice. (n = 5 mice per group) **e**, Total sample variation in dermal γδ T cells from naïve (white circles) and *N. brasiliensis*-infected (black circles) mice was summarised via PCA across all genes. **f**, DEGs from dermal γδ T cells were visualised using a volcano plot, genes significantly upregulated (red), and downregulated (blue) during *N. brasiliensis* infection were defined as having an adjusted *p* value of <0.05 or <0.1 and absolute log2 fold change of >1. **g**, Overrepresented gene ontology (GO): cellular components in DEGs from dermal γδ T cells from *N. brasiliensis*-infected (black circles) mice. **h**, Overrepresented GO: biological processes in upregulated genes in dermal γδ T cells from *N. brasiliensis*-infected (black circles) mice. **i**, overrepresented GO: biological processes in downregulated genes in dermal γδ T cells from *N. brasiliensis*-infected (black circles) mice. **j**, normalised counts for specific genes converted to Z-scores. **b,c**, Error bars represent mean±SD. Normality of the samples was assessed with Shapiro-Wilk normality test accordingly; statistical analysis was then performed using Student's t test or Mann-Whitney test. * $p < 0.05$; ** $p < 0.01$; *** $p < 0.001$; adjusted *p* value < 0.1

subsequent immune response. In particular, *N. brasiliensis* seems to first induce type-I and type-II IFN signalling together with type-2 immune responses. This response, which does not normally take place in the lungs, leads to uncontrolled inflammation and increased lung bleeding. Hence, the migration of dermal γδ17 T cells to the lungs can be seen as a host mechanism to fine-tune the immune response against the migrating larvae, ultimately aimed at maintaining tissue integrity. This host adaptation might also be beneficial to (and maybe even induced by) the parasite, as ensuring host survival guarantees the maintenance of a productive parasitic life cycle. Of note, *N. brasiliensis* larvae ex-sheath after going through the skin(32), enhancing parasite fitness. In contrast, i.v. infection bypasses this step, with larvae likely ex-sheathing in the bloodstream or directly in the lungs, exposing the cuticle as the primary source of PAMPs. This shift in PAMP availability possibly contributes to the change in the initial immune response towards a type-1 / type-2 bias.

An unexpected finding from this study was that IFN-γ, and not neutrophils, aggravates lung haemorrhage. We and others have previously shown that depleting neutrophils, or preventing their recruitment ameliorates the lung injury induced by *N. brasiliensis*(14, 15, 26). This notwithstanding, the data presented here indicates that the enhanced bleeding primarily stems from physical damage caused by the migrating larvae; with IFN-γ possibly affecting haemostatic pathways. Indeed, IFN-γ has been shown to increase vascular permeability both *in vitro* and *in vivo*(36, 37) and IFN-γ antibody blockade decreases acute lung injury in a murine flu infection model(28). Thus, our data suggests that upon encounter with the parasite in the skin dermal γδ17 T cells migrate to the lungs where they suppress, by yet unidentified mechanisms, type-1 effector subsets, preparing the tissue to avoid increased acute haemorrhagic damage. Interestingly, in the long term, IL-17-dependent neutrophilia induces emphysema-like lesions in the lungs(15).

In the dermis, we find almost exclusively IL-17-producing γδ T cells(19). Although dermal γδ17 T cells are activated early after parasite invasion, *N. brasiliensis* larvae do not induce their expansion or an increase in IL-17 production, as recently observed during *Schistosoma mansoni* infection(38). Instead, we observed an increase in the expression of genes related to cell movement, such as chemokine receptors and cell – extracellular matrix interactions. The activation signals driving migration of dermal γδ T cells are still unknown, but our previous data suggest that the increase in pulmonary γδ17 T cells is dependent on Ym1 and IL-1β(12), both of which are present in the *N. brasiliensis*-infected skin. Dermal γδ T cells are known to be a motile population that exhibits a steady migration rate between the skin tissue and draining lymph nodes(20, 33). Upon inflammation, these cells can even reach distal skin sites(33, 39), but to our knowledge γδ T cell migration from the skin to other mucosal organs has not yet been described. It is important to note, however, that γδ17 T cells from the gut have been shown to migrate to different organs(21, 40). Microbiota-activated small intestine γδ17 T cells migrate from the gut to the meninges during stroke and contribute to inflammation by recruiting neutrophils and monocytes(21). Similarly, small intestine memory γδ17 T cells were shown to migrate to the lungs during sepsis and contribute to acute lung injury through the production of IL-17A(40). Thus, it is conceivable that barrier-tissue-associated γδ17 T cells, particularly Vγ6$^+$ γδ T cells, might form a mucosal-wide network. Interestingly, data available in the literature seems to suggest that migratory γδ17 T cells tend to promote inflammation in distal organs(21, 40), whereas in our hands they act to maintain distal tissue integrity. A key difference is that during *N. brasiliensis* infection the pathogen is sequentially migrating through multiple organs, making the migration of γδ17 T cells a host adaptation to the parasite, whilst during sepsis and stroke a systemic inflammatory process is in place.

Irrespective of the functional consequences of γδ17 T cell migration (which seem to be highly context-dependent), our results suggest that the cellular make-up in non-lymphoid organs can be influenced by the immune events happening in distal sites. Our data further indicates that migration around mucosal sites occurs in steady state conditions as even in the absence of an infection skin-derived cells could be found in the lungs. However, topical tamoxifen treatment alone might induce a low-grade inflammatory insult in the skin triggering the migration of dermal γδ17 T cells to the lungs albeit at a lower migration rate than that induced by *N. brasiliensis* infection. The atopic march theory postulates that airway allergies (usually dependent on some form of type-2 immunity) arise from allergic responses taking place in the skin during early life(41). Thus, our results using an infectious trigger of type-2 immune responses could serve as a basis for iden-

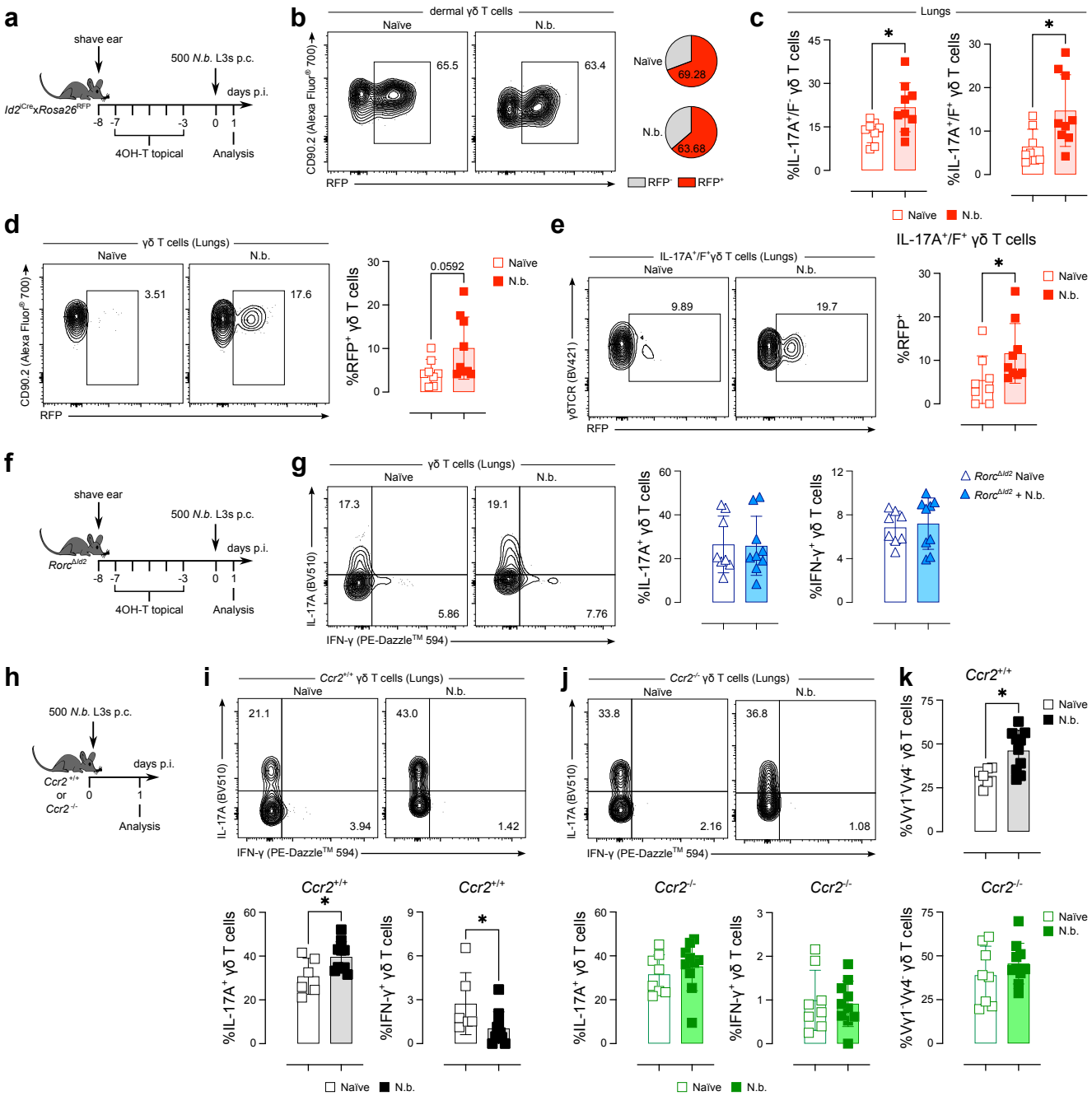

Fig. 5. Migratory dermal γδ17 T cells are responsible for the expansion in the lung γδ17 T cell population during *N. brasiliensis* infection. **a**, *Id2*^{CreERT2}x*Rosa26*^{RFP} mice had their right ear shaved, and starting on the following day were treated for five consecutive days with topical 4OH-T. Mice were then rested for 3 days before being infected with 500 *N. brasiliensis* L3s p.c. **b**, Flow cytometry analysis of RFP expression in dermal γδ T cells isolated from the skin of naïve and *N. brasiliensis*-infected. Summary pie charts showing the percentage of RFP$^+$ cells (red slice) within dermal γδ T cells (n = 11-13 mice per group; pool of 3 independent experiments). c, Summary graph showing the percentages of IL-17A$^+$IL-17F$^-$ and IL-17A$^+$IL-17F$^+$ cells within the γδ T cell population in the lungs of naïve (white squares) and *N. brasiliensis*-infected (red squares) mice (n = 8-9 mice per group; pool of 3 independent experiments). **d, e**, Flow cytometry analysis of RFP expression and summary graphs showing the percentage of RFP$^+$ cells within total γδ T cells (**d**) and IL-17A$^+$IL-17F$^+$ γδ T cells (**e**) isolated from the lungs of naïve (white squares) and *N. brasiliensis*-infected (red squares) mice. Summary graphs showing the percentage of RFP$^+$ cells within γδ T cells (n = 8-9 mice per group; pool of 3 independent experiments). **f**, *Id2*^{CreERT2}x*Rorc*$^{fl/fl}$ mice had their right ear shaved, and starting on the following day were treated for five consecutive days with topical 4OH-T. Mice were then rested for 3 days before being infected with 500 *N. brasiliensis* L3s p.c. **g**, Flow cytometry analysis of intracellular IL-17A and IFN-γ in γδ T cells isolated from the lungs of naïve (white triangles), and *N. brasiliensis*-infected (blue triangles) mice and stimulated *ex vivo* for 4h. Summary graph showing the percentages of IL-17A$^+$ and IFN-γ$^+$ cells within the γδ T cell population (n = 6-9 mice per group; pool of 2 independent experiments). **h**, *Ccr2*$^{-/-}$ and *Ccr2*$^{+/+}$ mice were infected 500 *N. brasiliensis* L3s p.c. and were analysed at day 1 p.i. **i, j**, Flow cytometry analysis of intracellular IL-17A and IFN-γ in γδ T cells isolated from the lungs of naïve (open squares) and *N. brasiliensis*-infected (filled squares) *Ccr2*$^{+/+}$ (**i**) and *Ccr2*$^{-/-}$ (**j**) mice and stimulated *ex vivo* for 4h. Summary graph showing the percentages of IL-17A$^+$ and IFN-γ$^+$ cells within γδ T cells (n = 6-10 mice per group; pool of 3 independent experiments). **k**, Summary graph showing the percentages Vγ1$^-$Vγ4$^-$ within γδ T cells isolated from the lungs of *Ccr2*$^{+/+}$ (top) and *Ccr2*$^{-/-}$ (bottom) mice (n = 6-10 mice per group; pool of 3 independent experiments). **c-l**, Error bars represent mean±SD. Normality of the samples was assessed with Shapiro-Wilk normality test; statistical analysis was then performed using Student's t test or Mann-Whitney test (**e, f**). * $p < 0.05$.

tifying mechanisms behind the atopic march. In particular, it would be interesting to determine if percutaneous allergen challenge promotes the migration of dermal γδ T cells, or other cell populations to the lungs. Overall, the unravelling of a skin – lung axis underlying inter-tissue communication during inflammatory responses opens exciting new avenues to understand immune responses at the whole-organismal level.

Methods

Mice and ethics

C57BL/6J^{crl} mice were obtained from Charles River. Id2$^{tm1.1(cre/ERT2)Blh}$; B6(Cg)-Rorc$^{tm3Litt/J}$; Gt(ROSA)26Sor^{Ai14} mice were originally provided by Dr. David Withers. Tcrd$^{tm1.1(cre/ERT2)Zhu}$ were kindly provided by Dr. Adrian Hayday. Ccr2^{tm1Ifc} (*Ccr2*$^{-/-}$) mice were kindly provided by Dr. Jo Konkel. *Ifngr*$^{-/-}$ mice were kindly provided by Dr. Lizzie Mann(42). Male and female mice were age- and sex-matched and housed in individually ventilated cages. Experimental mice were not randomised in cages, but each cage was randomly assigned to a treatment group. Mice were culled by asphyxiation in a rising concentration of CO_2. Experiments were performed in accordance with the United Kingdom Animals (Scientific Procedures) Act of 1986 (project license number 70/8547 and PP4115856).

N. brasiliensis *infection*

N. brasiliensis was maintained by serial passage through Sprague-Dawley rats, as described previously(43). Third-stage larvae (L3) were isolated from the clean edges of parasite cultures and washed five times with PBS (Dulbecco's PBS, Sigma) before infection. On day 0, mice were infected percutaneously with 500 L3 larvae on the right ear, as described in the results section. At various time points mice were euthanised and BAL and lungs were taken for further analysis. On day 1 p.i., BAL fluid absorbance was measured at 400nm using a VersaMax microplate reader (Molecular Devices) to assess lung haemorrhage(44). For lung-stage L4 counts on days 1 and 2 p.i., lungs were minced and incubated in PBS for 24h at 37°C; emergent larvae were counted using a dissecting microscope. For gut worm counts, small intestines of infected mice were collected in PBS, and were then cut longitudinally along the entire length, placed in gauze in a 50ml Falcon and incubated at 37°C for 3 to 4h, settled worms were then counted with the aid of a dissecting microscope.

Histology and immunofluorescence staining

For histology, ears were collected in PBS and fixed in formalin for 24h before transferring to 70% ethanol. Tissues were processed, embedded in paraffin, and then sectioned (5 µm thickness) onto glass microscopy slides (Superfrost Plus Adhesion slides, J1830AMNZ, Thermo Fisher Scientific). For immunostaining, lung sections were deparaffinised, rehydrated and heat-mediated antigen retrieval performed using Tris-EDTA buffer (10 mM Tris, 1 mM EDTA), pH 9.0 (20 mins incubation at 95°C). Tissue sections were permeabilised in 1% Triton-X100 in PBS (10 mins at room temperature) and then non-specific protein-binding blocked (10% normal donkey serum, 1% BSA, 0.05% Tween-20 in PBS, 30 minutes at room temperature) before sections were incubated with primary antibody overnight at 4°C. All sections were washed in PBS with 0.05% Tween-20 followed by PBS before incubation with secondary antibody (donkey anti-rabbit NorthernLights™ NL637-conjugated antibody, 1:200, NL005; R&D Systems, or streptavidin NL557-conjugated, 1:800, NL999, R&D Systems) for 1 hour at room temperature. Sections were washed as before, incubated with 4,6-diamidino-2-phenylindole (DAPI, 1:40,000 in PBS, 2 mins at room temperature) and then mounted (Fluorescence mounting medium, S3023, Agilent Technologies) and cover-slipped. Staining was visualised on an Olympus IX83 deconvolution microscope.

Cell preparation, flow cytometry, and analysis

BAL was collected in a 15mL Falcon tube by washing the airways of euthanised mice 4 times with 0.4 mL of PBS. Cells were centrifuged at 400 x g for 5 mins, the supernatant was either discarded or collected for further analysis; cells were then resuspended in PBS containing 1% FBS and 0.2 µM EDTA. Ears were dissected, and the two ear sheets were split with the help of a pair of forceps. Split ear sheets were then digested with Liberase (0.25 mg/mL; Roche) and DNase I (0.5 mg/mL; Sigma-Aldrich) in 0.5mL RPMI 1640 at 37°C, 200 rpm, for 1h 45 mins. The supernatant and the remainder of the tissue were added to a Medicon (BD Biosciences) then homogenised with the help of a Medimachine for 5 minutes. The resulting tissue homogenate was then passed through a 70-µm cell strainer and washed in 10mL of RPMI 1640 containing 10% Fetal Bovine Serum (FBS). Lungs were dissected and tissue was cut into pieces, then digested with Liberase (0.4 U/mL; Roche) and DNase I (80 U/ml) (Thermofisher) in RPMI 1640 at 37°C for 45 mins. Single cells were isolated by passing the tissue through a 70-µm cell strainer. Cells were washed in 10mL of RPMI 1640 containing 10% FBS. For lung samples, red blood cells were lysed using an ammonium-chloride-potassium (ACK) buffer (Gibco) for 3mins at room temperature and reaction was stopped by diluting samples in PBS. Total BAL, ear and lung live cells were counted with AO/PI dye on an automated cell counter (Auto2000, Nexcelom). Cells were then incubated with anti-CD16/CD32 5 µg/ml (Mouse Fc Block, BD) and LIVE/DEAD Blue (ThermoFisher) in PBS for 15 mins. Next, cells were incubated, without washing, with antibodies to surface antigens for further 15 minutes. After incubation cells were washed with PBS containing 1% FBS and 0.2 µM of EDTA and fixed with eBioscienceTM IC Fixation Buffer (Invitrogen) – or BD Cytofix™ Fixation Buffer (BD Biosciences) for cells expressing fluorescent proteins – for 20 minutes. Optionally, for intracellular cytokine staining, after tissue digestion and cell counting, cells were incubated in a 96 round-bottom wells plate in a 2-3x10^6 cells/well concentration with a cell stimulation cocktail containing protein transport inhibitor (eBioscience) for 3h to 4h at 37°C.

Cells were then stained for surface markers as described above, fixed for 30 mins at 4°C and permeabilised with the Foxp3/Transcription Factor Staining Buffer set (eBioscience) – or fixed with BD Cytofix™ Fixation Buffer (BD Biosciences) for cells expressing fluorescent proteins – and finally incubated overnight at 4°C with cytokine-specific antibodies in permeabilization buffer (eBioscience). Cells were analysed using either a FACSFortessa or a FACSymphony (both BD Biosciences) and analysed using FlowJo software (v10; Tree Star).

Immuno-detection of cytokines in lung tissue samples

Ear tissue was homogenised in 2 mL sterile tubes containing 600 µL PBS plus a cocktail of protease inhibitors (cOmplete ULTRA tablets, Mini; Roche) and metal beads (BioSpec Products), with the help of a TissueLyzer II tissue homogenizer (Qiagen). The homogenate was centrifuged at 10000 x g to remove cellular debris and beads and stored at -80ºC until usage. Cytokine concentrations were assessed using LEGENDplex™ Mouse Th1/Th2 and Mouse Cytokine Panel 2 kits – both bead-based assays that use the principles of sandwich ELISA to quantify soluble analytes using a flow cytometer (Biolegend) – according to manufacturer's instruction. Cytokine concentrations were normalised using total protein concentration in tissue homogenate, determined in a NanoDrop spectrophotometer (ThermoFisher).

Nanostring RNA profiling

Lung and ear tissue were homogenised in 2 mL sterile tubes containing 300 µL of lysis buffer (Qiagen), with the help of a TissueLyzer II tissue homogenizer (Qiagen). mRNA was then prepared from tissue homogenates using the RNeasy® Mini Kit (Qiagen). Extracted RNA was then diluted to 20ng/µL in RNase free H2O, measured using Qubit™ RNA HS Assay Kit (Thermofisher) and run on a Nanostring nCounter® FLEX system using the Mouse Host Response (V1) and Mouse Myeloid Innate Immunity (V2) panels as specified in legends as per manufacturer's instructions. Raw data were loaded into nSolver version 4.0 using default settings. Non-normalised counts were then exported, and subsequent analyses were performed in R (v3.6) using RStudio (v1.2.1335 Build 1379). Positive controls were analysed to ensure there was clear resolution at variable expression levels and negative controls were used to set a minimum detection threshold which was applied to all samples. Data were then normalised with edgeR (v4.0) using the TMM method and differential expression between *N. brasiliensis*-infected and naïve mice, or p.c.- and i.v.-infected mice, was calculated via linear modelling with empirical Bayes smoothing using the limma R package (v2.43). Genes with an absolute fold change of greater than one and a significance value of under 0.05 were defined as "differentially expressed" and taken forward for further analysis. PCA and Volcano plots were then generated from normalised counts and fold changes of DEGs using the ggplot2 R package (v3.5.1). The networks and functional analyses of DEGs were generated either via the clusterProfiler (v4.10.1) and enrichplot (v1.22.0) packages, or using the Ingenuity Pathway Analysis software (IPA; QIAGEN Inc., https://www.qiagenbioinformatics.com/products/ingenuity-pathway-analysis); for the latter, data were then imported into R for visualisation.

Cell sorting

For cell sorting of lung innate-like lymphocytes, lung tissue was digested as described above and, additionally, single cells were isolated by passing the tissue through a 40-µm cell strainer, followed by a 70% / 30% Percoll (Sigma-Aldrich) gradient and 30-min centrifugation at 2400 rpm. Leukocytes were recovered from the interface, resuspended, and immunostained as described above. Up to 10,000 γδ T cells and Lin$^-$Thy1.2$^+$ cells (defined as CD45$^+$CD64$^-$CD11b$^-$CD11c$^-$MHC-II$^-$B220$^-$Thy1.2$^+$CD4$^-$γδTCR$^{+/-}$), 2,500 NK1.1$^+$γδTCR$^-$ innate lymphocytes (defined as CD45$^+$CD64$^-$CD11b$^-$CD11c$^-$MHC-II$^-$B220$^-$Thy1.2$^+$CD4$^-$γδTCR$^-$), and 2,500 NK cells (defined as CD45$^+$Thy1.2$^-$NK1.1$^+$) per mouse were then sorted on a FACSAria (BD Biosciences) into sterile RNase-free 2 mL tubes containing RPMI 1640 with 10% FBS. The cell populations sorted from 4 mice per group were then pooled post-sorting in one Eppendorf containing PBS with 10

Single cell isolation and library construction

Gene expression libraries were prepared from single cells using the Chromium Controller and Single Cell 3 Reagent Kits v3.1 (10x Genomics, Inc. Pleasanton, USA) according to the manufacturer's protocol (CG000315 Rev C). Briefly, nanoliter-scale Gel Beads-in-emulsion (GEMs) were generated by combining barcoded Gel Beads, a master mix containing cells, and partitioning oil onto a Chromium chip. Cells were delivered at a limiting dilution, such that the majority (90-99%) of generated GEMs contain no cell, while the remainder largely contain a single cell. The Gel Beads were then dissolved, primers released, and any co-partitioned cells lysed. Primers containing an Illumina TruSeq Read 1 sequencing primer, a 16-nucleotide 10x Barcode, a 10-nucleotide unique molecular identifier (UMI) and a 30-nucleotide poly(dT) sequence were then mixed with the cell lysate and a master mix containing reverse transcription (RT) reagents. Incubation of the GEMs then yielded barcoded cDNA from poly-adenylated mRNA. Following incubation, GEMs were broken and pooled fractions recovered. First-strand cDNA was then purified from the post GEM-RT reaction mixture using silane magnetic beads and amplified via PCR to generate sufficient mass for library construction. Enzymatic fragmentation and size selection were then used to optimize the cDNA amplicon size. Illumina P5 & P7 sequences, a sample index, and TruSeq Read 2 sequence were added via end repair, A-tailing, adaptor ligation, and PCR to yield final Illumina-compatible sequencing libraries.

Single Cell RNA Sequencing

The resulting sequencing libraries comprised standard Illumina paired-end constructs flanked with P5 and P7 se-

quences. The 16 bp 10x Barcode and 10 bp UMI were encoded in Read 1, while Read 2 was used to sequence the cDNA fragment. Sample index sequences were incorporated as the i7 index read. Paired-end sequencing (28:90) was performed on the Illumina NovaSeq6000 platform.

Data pre-processing

Raw data files generated from the sequencing instrument were processed using 10x Genomics Cell Ranger pipeline (v7.1.0). Base call (BCL) files were demultiplexed and converted to FASTQ files using "cellranger mkfastq". The FASTQ files were then mapped to the pre-built Mouse reference package from 10x Genomics (mm10-2020-A) using "cellranger count" to produce the feature-barcode matrices.

Single cell data analysis

The single-cell data were processed in R environment (v4.3) following the workflow documented in Orchestrating Single-Cell Analysis with Bioconductor(45). Briefly, for each sample, the HDF5 file generated by Cell Ranger was imported into R to create a SingleCellExperiment object. A combination of median absolute deviation (MAD), as implemented by the "isOutlier" function in the scuttle R package (v1.12.0) and exact thresholds was used to identify and subsequently remove low quality cells before data integration. The log-normalised expression values of the combined data were computed using the "multiBatchNorm" function from the batchelor R package (v1.18.1). The per-gene variance of the log-expression profile was modelled using the "modelGeneVarByPoisson" function from the scran R package (v1.30.2) and top 5,000 highly variable genes were selected. The mutual nearest neighbors (MNN) approach implemented by the "fastMNN" function from the batchelor R package was used to perform batch correction. The first 50 dimensions of the MNN low-dimensional corrected coordinates for all cells were used as input to produce the t-stochastic neighbour embedding (t-SNE) projection and uniform manifold approximation and projection (UMAP) using the "runTSNE" and "runUMAP" functions from the scater R package (v1.30.1) respectively. The Leiden algorithm from the igraph R package (v2.0.2) was used to perform a first-pass clustering, followed by clustering using the Louvain algorithm to produce 39 putative cell clusters. Through manual curation, the cells were grouped into 20 clusters, including one consisting of doublet cells. Differential expression analysis of the 3 treatment groups (control, *N. brasiliensis* infection via skin contact and infected intravenously) across clusters was performed using DESeq2 R package (v 1.43.4), with recommended parameters. Genes with a false discovery rate (FDR) below 5% were considered differentially expressed. To calculate a "Type-1 module score", the combined per-cell mean expression of candidate type-1 effector molecules extracted from the literature(29–31) was calculated using the "colMeans" function in the gmatrix R package.

Bulk RNA sequencing

For cell sorting of dermal γδ T cells and DETCs, skin tissue was digested as described above and, additionally, single cells were isolated by passing the tissue through a 40-µm cell strainer, followed by a 70% / 30% Percoll (Sigma-Aldrich) gradient and 30-min centrifugation at 2400 rpm. Leukocytes were recovered from the interface, resuspended, and immunostained as described above. Dermal γδ T cells were defined as $CD45^+CD64^-CD11b^-CD11c^-MHC\text{-}II^-Fc\varepsilon R1^-Thy1.2^+CD3^+\gamma\delta TCR^+V\gamma5^-$, DETCs were defined as $CD45^+CD64^-CD11b^-CD11c^-MHC\text{-}II^-Fc\varepsilon R1^-Thy1.2^+CD3^+\gamma\delta TCR^+V\gamma5^+$ and then electronically sorted on a FACSAria (BD Biosciences) into sterile RNase-free Eppendorfs containing 200µL of lysis buffer (Qiagen), for posterior mRNA isolation; each mouse was treated as one individual sample. RNA was then isolated from sorted cells using the Single Cell RNA Purification Kit (Norgen). Samples were sent to Novogene Company Limited (Cambridge, UK) where QC checks and sequencing were performed. mRNA pre-amplification was employed using the SMARTer kit (Takara Bio) prior to library preparation by poly(A) enrichment and paired-end sequenced on an Illumina NovaSeq 6000 for 300 cycles (2 x 150 bp). FASTQ files were received, which were then aligned to GENCODE mouse genome (version M33, Jan 2020), and quantified using Salmon software (v1.10.3) using –validatemappings and –gcBias flags (COMBINE-lab). Annotated and quantified data was then imported into RStudio (v2022.07.2+576) using the Tximeta R package (v4.2.3). Genes with an average raw count of less than ten across all groups were removed. Principal component analysis (PCA) was used to summarise total variation within the dataset. Differential expression analysis was performed using the DESeq2 R package (v1.46.0) and volcano plots and dot plots were then generated using ggplot2 R package (v3.5.1). The networks and functional analyses of DEGs were generated either via the clusterProfiler (v4.10.1) and enrichplot (v1.22.0) packages or via import into PANTHER (v19.0) via the web GUI (https://geneontology.org).

In vivo *substance administration*

For FTY720 experiments, FTY720 (Sigma-Aldrich) was administered in the drinking water (final concentration of 2.5 µg/mL) three days before infection. Water pouches were replaced after three days with freshly prepared FTY720 added each time.

Statistics

Prism 9.5.1 and 10.4.0 (versions 9 and 10, respectively; GraphPad Software Inc) were used for statistical analysis. Data were tested for normality using the Shapiro-Wilk test and then differences between experimental groups were assessed accordingly. For gene expression data, normalised expression values were log2 transformed to achieve normal distribution. Comparisons with a p value<0.05 (unless stated otherwise) were considered to be statistically significant. Data are represented as mean±SD.

ACKNOWLEDGEMENTS

We thank the staff at the Biological Services Facility, Flow Cytometry Facility and Genomics Facility – in particular David Chapman and Claire Morrisroe – at The University of Manchester. We are also grateful to Novogene for the services provided. We thank Miguel Muñoz-Ruiz, Kara Filbey, Jesuthas Ajendra, Alistair Chenery, Conor Finlay, Tara Sutherland, Dominik Rückerl, Suzie Hodge, Roser Tachó-Piñot, Kelly Wemyss, Lizzie Mann and Abdullah Shazad for helpful discussions, sharing of resources and technical advice. Finally, we thank Prof. Bruno Silva-Santos for carefully reading the manuscript. This work was funded by the Wellcome Trust (106898/A/15/Z) and MRC (MR/V011235/1) to J.E.A., European Molecular Biology Organization (LTF 191-2019) and European Commission Marie Sklodowska-Curie Individual Fellowship (ref. 101025781) to P.H.P.; Sir Henry Dale Fellowship (jointly funded by the Wellcome Trust and the Royal Society; 105644/Z/14/Z) and BBSRC (BB/T014482/1) to M.R.H.

AUTHOR CONTRIBUTIONS

Conceptualization: P.H.P. and J.E.A.; Methodology and Investigation: P.H.P., J.E.P., B.H.K.C., G.E.B., F.D., L.Z., R.J.D., S.T.P., N.F., M.R.H.; Data Analysis: P.H.P., J.E.P. and I-H.L.; Resources: D.R.W. and J.E.K.; Writing – original draft: P.H.P. and J.E.A.; Writing – review and editing: P.H.P., J.E.P., J.E.K., M.R.H., and J.E.A.

COMPETING FINANCIAL INTERESTS

The authors declare no conflicts of interest.

References

1. H. Veiga-Fernandes and A. A. Freitas. The s(c)ensory immune system theory. *Trends Immunol*, 38(10):777–788, 2017. doi: 10.1016/j.it.2017.02.007.
2. J. E. Allen, T. E. Sutherland, and D. Ruckerl. Il-17 and neutrophils: unexpected players in the type 2 immune response. *Curr Opin Immunol*, 34:99–106, 2015. doi: 10.1016/j.coi.2015.03.001.
3. R. M. Maizels and W. C. Gause. Targeting helminths: The expanding world of type 2 immune effector mechanisms. *J Exp Med*, 220(10), 2023. doi: 10.1084/jem.20221381.
4. W. C. Gause, T. A. Wynn, and J. E. Allen. Type 2 immunity and wound healing: evolutionary refinement of adaptive immunity by helminths. *Nat Rev Immunol*, 13(8):607–14, 2013. doi: 10.1038/nri3476.
5. J. E. Allen. Il-4 and il-13: Regulators and effectors of wound repair. *Annu Rev Immunol*, 41: 229–254, 2023. doi: 10.1146/annurev-immunol-101921-041206.
6. S. Z. Hasnain, H. Wang, J. E. Ghia, N. Haq, Y. Deng, A. Velcich, R. K. Grencis, D. J. Thornton, and W. I. Khan. Mucin gene deficiency in mice impairs host resistance to an enteric parasitic infection. *Gastroenterology*, 138(5):1763–71, 2010. doi: 10.1053/j.gastro.2010.01.045.
7. A. Zhao, J. McDermott, Jr. Urban, J. F., W. Gause, K. B. Madden, K. A. Yeung, S. C. Morris, F. D. Finkelman, and T. Shea-Donohue. Dependence of il-4, il-13, and nematode-induced alterations in murine small intestinal smooth muscle contractility on stat6 and enteric nerves. *J Immunol*, 171(2):948–54, 2003. doi: 10.4049/jimmunol.171.2.948.
8. R. J. Dodd, D. Moffatt, M. Vachiteva, J. E. Parkinson, B. H. K. Chan, A. J. Day, J. E. Allen, and T. E. Sutherland. Injury from nematode lung migration induces an il-13-dependent hyaluronan matrix. *Proteoglycan Res*, 2(4):e70012, 2024. doi: 10.1002/pgr2.70012.
9. M. G. Chiaramonte, D. D. Donaldson, A. W. Cheever, and T. A. Wynn. An il-13 inhibitor blocks the development of hepatic fibrosis during a t-helper type 2-dominated inflammatory response. *J Clin Invest*, 104(6):777–85, 1999. doi: 10.1172/JCI7325.
10. T. Bouchery, B. Volpe, K. Shah, L. Lebon, K. Filbey, G. LeGros, and N. Harris. The study of host immune responses elicited by the model murine hookworms nippostrongylus brasiliensis and heligmosomoides polygyrus. *Curr Protoc Mouse Biol*, 7(4):236–286, 2017. doi: 10.1002/cpmo.34.
11. Jr. Urban, J. F., N. Noben-Trauth, D. D. Donaldson, K. B. Madden, S. C. Morris, M. Collins, and F. D. Finkelman. Il-13, il-4ralpha, and stat6 are required for the expulsion of the gastrointestinal nematode parasite nippostrongylus brasiliensis. *Immunity*, 8(2):255–64, 1998. doi: 10.1016/s1074-7613(00)80477-x.
12. T. E. Sutherland, N. Logan, D. Ruckerl, A. A. Humbles, S. M. Allan, V. Papayannopoulos, B. Stockinger, R. M. Maizels, and J. E. Allen. Chitinase-like proteins promote il-17-mediated neutrophilia in a tradeoff between nematode killing and host damage. *Nat Immunol*, 15(12): 1116–25, 2014. doi: 10.1038/ni.3023.
13. J. Ajendra, A. L. Chenery, J. E. Parkinson, B. H. K. Chan, S. Pearson, S. A. P. Colombo, L. Boon, R. K. Grencis, T. E. Sutherland, and J. E. Allen. Il-17a both initiates, via ifngamma suppression, and limits the pulmonary type-2 immune response to nematode infection. *Mucosal Immunol*, 13(6):958–968, 2020. doi: 10.1038/s41385-020-0318-2.
14. J. Ajendra, P. H. Papotto, J. E. Parkinson, R. J. Dodd, A. L. Bombeiro, S. Pearson, B. H. K. Chan, J. C. Ribot, H. J. McSorley, T. E. Sutherland, and J. E. Allen. The il-17a-neutrophil axis promotes epithelial cell il-33 production during nematode lung migration. *Mucosal Immunol*, 16(6):767–775, 2023. doi: 10.1016/j.mucimm.2023.09.006.
15. F. Chen, W. Wu, L. Jin, A. Millman, M. Palma, D. W. El-Naccache, K. E. Lothstein, C. Dong, K. L. Edelblum, and W. C. Gause. B cells produce the tissue-protective protein relmalpha during helminth infection, which inhibits il-17 expression and limits emphysema. *Cell Rep*, 25(10):2775–2783 e3, 2018. doi: 10.1016/j.celrep.2018.11.038.
16. D. A. Ferrick, M. D. Schrenzel, T. Mulvania, B. Hsieh, W. G. Ferlin, and H. Lepper. Differential production of interferon-gamma and interleukin-4 in response to th1- and th2-stimulating pathogens by gamma delta t cells in vivo. *Nature*, 373(6511):255–7, 1995. doi: 10.1038/373255a0.
17. J. C. Ribot, A. deBarros, D. J. Pang, J. F. Neves, V. Peperzak, S. J. Roberts, M. Girardi, J. Borst, A. C. Hayday, D. J. Pennington, and B. Silva-Santos. Cd27 is a thymic determinant of the balance between interferon-gamma- and interleukin 17-producing gammadelta t cell subsets. *Nat Immunol*, 10(4):427–36, 2009. doi: 10.1038/ni.1717.
18. P. H. Papotto, J. C. Ribot, and B. Silva-Santos. Il-17(+) gammadelta t cells as kick-starters of inflammation. *Nat Immunol*, 18(6):604–611, 2017. doi: 10.1038/ni.3726.
19. N. Sumaria, B. Roediger, L. G. Ng, J. Qin, R. Pinto, L. L. Cavanagh, E. Shklovskaya, B. Fazekas de St Groth, J. A. Triccas, and W. Weninger. Cutaneous immunosurveillance by self-renewing dermal gammadelta t cells. *J Exp Med*, 208(3):505–18, 2011. doi: 10.1084/jem.20101824.
20. E. E. Gray, K. Suzuki, and J. G. Cyster. Cutting edge: Identification of a motile il-17-producing gammadelta t cell population in the dermis. *J Immunol*, 186(11):6091–5, 2011. doi: 10.4049/jimmunol.1100427.
21. C. Benakis, D. Brea, S. Caballero, G. Faraco, J. Moore, M. Murphy, G. Sita, G. Racchumi, L. Ling, E. G. Pamer, C. Iadecola, and J. Anrather. Commensal microbiota affects ischemic stroke outcome by regulating intestinal gammadelta t cells. *Nat Med*, 22(5):516–23, 2016. doi: 10.1038/nm.4068.
22. P. H. Papotto, B. Yilmaz, and B. Silva-Santos. Crosstalk between gammadelta t cells and the microbiota. *Nat Microbiol*, 6(9):1110–1117, 2021. doi: 10.1038/s41564-021-00948-2.
23. D. L. Lee. Penetration of mammalian skin by the infective larva of nippostrongylus brasiliensis. *Parasitology*, 65(3):499–505, 1972. doi: 10.1017/s0031182000044115.
24. L. M. Connor, S. C. Tang, E. Cognard, S. Ochiai, K. L. Hilligan, S. I. Old, C. Pellefigues, R. F. White, D. Patel, A. A. Smith, D. A. Eccles, O. Lamiable, M. J. McConnell, and F. Ronchese. Th2 responses are primed by skin dendritic cells with distinct transcriptional profiles. *J Exp Med*, 214(1):125–142, 2017. doi: 10.1084/jem.20160470.
25. C. Pellefigues, S. C. Tang, A. Schmidt, R. F. White, O. Lamiable, L. M. Connor, C. Ruedl, J. Dobrucki, G. Le Gros, and F. Ronchese. Toll-like receptor 4, but not neutrophil extracellular traps, promote ifn type i expression to enhance th2 responses to nippostrongylus brasiliensis. *Front Immunol*, 8:1575, 2017. doi: 10.3389/fimmu.2017.01575.
26. F. Chen, Z. Liu, W. Wu, C. Rozo, S. Bowdridge, A. Millman, N. Van Rooijen, Jr. Urban, J. F., T. A. Wynn, and W. C. Gause. An essential role for th2-type responses in limiting acute tissue damage during experimental helminth infection. *Nat Med*, 18(2):260–6, 2012. doi: 10.1038/nm.2628.
27. H. Nagashima, T. Mahlakoiv, H. Y. Shih, F. P. Davis, F. Meylan, Y. Huang, O. J. Harrison, C. Yao, Y. Mikami, Jr. Urban, J. F., K. M. Caron, Y. Belkaid, Y. Kanno, D. Artis, and J. J. O'Shea. Neuropeptide cgrp limits group 2 innate lymphoid cell responses and constrains type 2 inflammation. *Immunity*, 51(4):682–695 e6, 2019. doi: 10.1016/j.immuni.2019.06.009.
28. B. Liu, L. Bao, L. Wang, F. Li, M. Wen, H. Li, W. Deng, X. Zhang, and B. Cao. Anti-ifn-gamma therapy alleviates acute lung injury induced by severe influenza a (h1n1) pdm09 infection in mice. *J Microbiol Immunol Infect*, 54(3):396–403, 2021. doi: 10.1016/j.jmii.2019.07.009.
29. L. Mazzurana, P. Czarnewski, V. Jonsson, L. Wigge, M. Ringner, T. C. Williams, A. Ravindran, A. K. Bjorklund, J. Safholm, G. Nilsson, S. E. Dahlen, A. C. Orre, M. Al-Ameri, C. Hoog, C. Hedin, S. Szczegielniak, S. Almer, and J. Mjosberg. Tissue-specific transcriptional imprinting and heterogeneity in human innate lymphoid cells revealed by full-length single-cell rna-sequencing. *Cell Res*, 31(5):554–568, 2021. doi: 10.1038/s41422-020-00445-x.
30. A. P. McFarland, A. Yalin, S. Y. Wang, V. S. Cortez, T. Landsberger, R. Sudan, V. Peng, H. L. Miller, B. Ricci, E. David, R. Faccio, I. Amit, and M. Colonna. Multi-tissue single-cell analysis deconstructs the complex programs of mouse natural killer and type 1 innate lymphoid cells in tissues and circulation. *Immunity*, 54(6):1320–1337 e4, 2021. doi: 10.1016/j.immuni.2021.03.024.
31. R. Wiesheu, S. C. Edwards, A. Hedley, H. Hall, M. Tosolini, M. G. F. Fares da Silva, N. Sumaria, S. M. Castenmiller, L. Wardak, Y. Optaczy, A. Lynn, D. G. Hill, A. J. Hayes, J. Hay, A. Kilbey, R. Shaw, D. Whyte, P. J. Walsh, A. M. Michie, G. J. Graham, A. Manoharan, C. Halsey, K. Blyth, M. C. Wolkers, C. Miller, D. J. Pennington, G. W. Jones, J. J. Fournie, V. Bekiaris, and S. B. Coffelt. Il-27 maintains cytotoxic ly6c(+) gammadelta t cells that arise from immature precursors. *EMBO J*, 43(14):2878–2907, 2024. doi: 10.1038/s44318-024-00133-1.
32. T. Bouchery, M. Moyat, J. Sotillo, S. Silverstein, B. Volpe, G. Coakley, T. D. Tsourouktsoglou, L. Becker, K. Shah, M. Kulagin, R. Guiet, M. Camberis, A. Schmidt, A. Seitz, P. Giacomin, G. Le Gros, V. Papayannopoulos, A. Loukas, and N. L. Harris. Hookworms evade host immunity by secreting a deoxyribonuclease to degrade neutrophil extracellular traps. *Cell Host Microbe*, 27(2):277–289 e6, 2020. doi: 10.1016/j.chom.2020.01.011.
33. F. Ramirez-Valle, E. E. Gray, and J. G. Cyster. Inflammation induces dermal vgamma4+ gammadeltat17 memory-like cells that travel to distant skin and accelerate secondary il-17-driven responses. *Proc Natl Acad Sci U S A*, 112(26):8046–51, 2015. doi: 10.1073/pnas.1508990112.
34. D. R. McKenzie, E. E. Kara, C. R. Bastow, T. S. Tyllis, K. A. Fenix, C. E. Gregor, J. J. Wilson, R. Babb, J. C. Paton, A. Kallies, S. L. Nutt, A. Brustle, M. Mack, I. Comerford, and S. R. McColl. Il-17-producing gammadelta t cells switch migratory patterns between resting and activated states. *Nat Commun*, 8:15632, 2017. doi: 10.1038/ncomms15632.
35. P. Matzinger and T. Kamala. Tissue-based class control: the other side of tolerance. *Nat Rev Immunol*, 11(3):221–30, 2011. doi: 10.1038/nri2940.
36. C. T. Ng, L. Y. Fong, M. R. Sulaiman, M. A. Moklas, Y. K. Yong, M. N. Hakim, and Z. Ahmad. Interferon-gamma increases endothelial permeability by causing activation of p38 map kinase and actin cytoskeleton alteration. *J Interferon Cytokine Res*, 35(7):513–22, 2015. doi: 10.1089/jir.2014.0188.
37. V. Langer, E. Vivi, D. Regensburger, T. H. Winkler, M. J. Waldner, T. Rath, B. Schmid, L. Skottke, S. Lee, N. L. Jeon, T. Wohlfahrt, V. Kramer, P. Tripal, M. Schumann, S. Kersting, C. Handtrack, C. I. Geppert, K. Suchowski, R. H. Adams, C. Becker, A. Ramming, E. Naschberger, N. Britzen-Laurent, and M. Sturzl. Ifn-gamma drives inflammatory bowel disease pathogenesis through ve-cadherin-directed vascular barrier disruption. *J Clin Invest*, 129(11):4691–4707, 2019. doi: 10.1172/JCI124884.
38. J. M. Inclan-Rico, C. M. Napuri, C. Lin, L. Y. Hung, A. A. Ferguson, X. Liu, Q. Wu, C. F. Pastore, A. Stephenson, U. M. Femoe, F. Musaigwa, H. L. Rossi, B. D. Freedman, D. R. Reed, T. Machacek, P. Horak, I. Abdus-Saboor, W. Luo, and D. R. Herbert. Mrgpra3 neurons drive cutaneous immunity against helminths through selective control of myeloid-derived il-

33. *Nat Immunol*, 25(11):2068–2084, 2024. doi: 10.1038/s41590-024-01982-y.
39. T. Hartwig, S. Pantelyushin, A. L. Croxford, P. Kulig, and B. Becher. Dermal il-17-producing gammadelta t cells establish long-lived memory in the skin. *Eur J Immunol*, 45(11):3022–33, 2015. doi: 10.1002/eji.201545883.
40. B. Xie, M. Wang, X. Zhang, Y. Zhang, H. Qi, H. Liu, Y. Wu, X. Wen, X. Chen, M. Han, D. Xu, X. Sun, X. Zhang, X. Zhao, Y. Shang, S. Yuan, and J. Zhang. Gut-derived memory gammadelta t17 cells exacerbate sepsis-induced acute lung injury in mice. *Nat Commun*, 15(1):6737, 2024. doi: 10.1038/s41467-024-51209-9.
41. D. A. Hill and J. M. Spergel. The atopic march: Critical evidence and clinical relevance. *Ann Allergy Asthma Immunol*, 120(2):131–137, 2018. doi: 10.1016/j.anai.2017.10.037.
42. H. M. Lee, A. Fleige, R. Forman, S. Cho, A. A. Khan, L. L. Lin, D. T. Nguyen, A. O'Hara-Hall, Z. Yin, C. A. Hunter, W. Muller, and L. F. Lu. Ifngamma signaling endows dcs with the capacity to control type i inflammation during parasitic infection through promoting t-bet+ regulatory t cells. *PLoS Pathog*, 11(2):e1004635, 2015. doi: 10.1371/journal.ppat.1004635.
43. M. Camberis, G. Le Gros, and Jr. Urban, J. Animal model of nippostrongylus brasiliensis and heligmosomoides polygyrus. *Curr Protoc Immunol*, Chapter 19:Unit 19 12, 2003. doi: 10.1002/0471142735.im1912s55.
44. E. Dahlberg. Estimation of the blood contamination of tissue extracts. *Anal Biochem*, 130 (1):108–13, 1983. doi: 10.1016/0003-2697(83)90656-5.
45. R. A. Amezquita, A. T. L. Lun, E. Becht, V. J. Carey, L. N. Carpp, L. Geistlinger, F. Marini, K. Rue-Albrecht, D. Risso, C. Soneson, L. Waldron, H. Pages, M. L. Smith, W. Huber, M. Morgan, R. Gottardo, and S. C. Hicks. Orchestrating single-cell analysis with bioconductor. *Nat Methods*, 17(2):137–145, 2020. doi: 10.1038/s41592-019-0654-x.

Supplementary Information

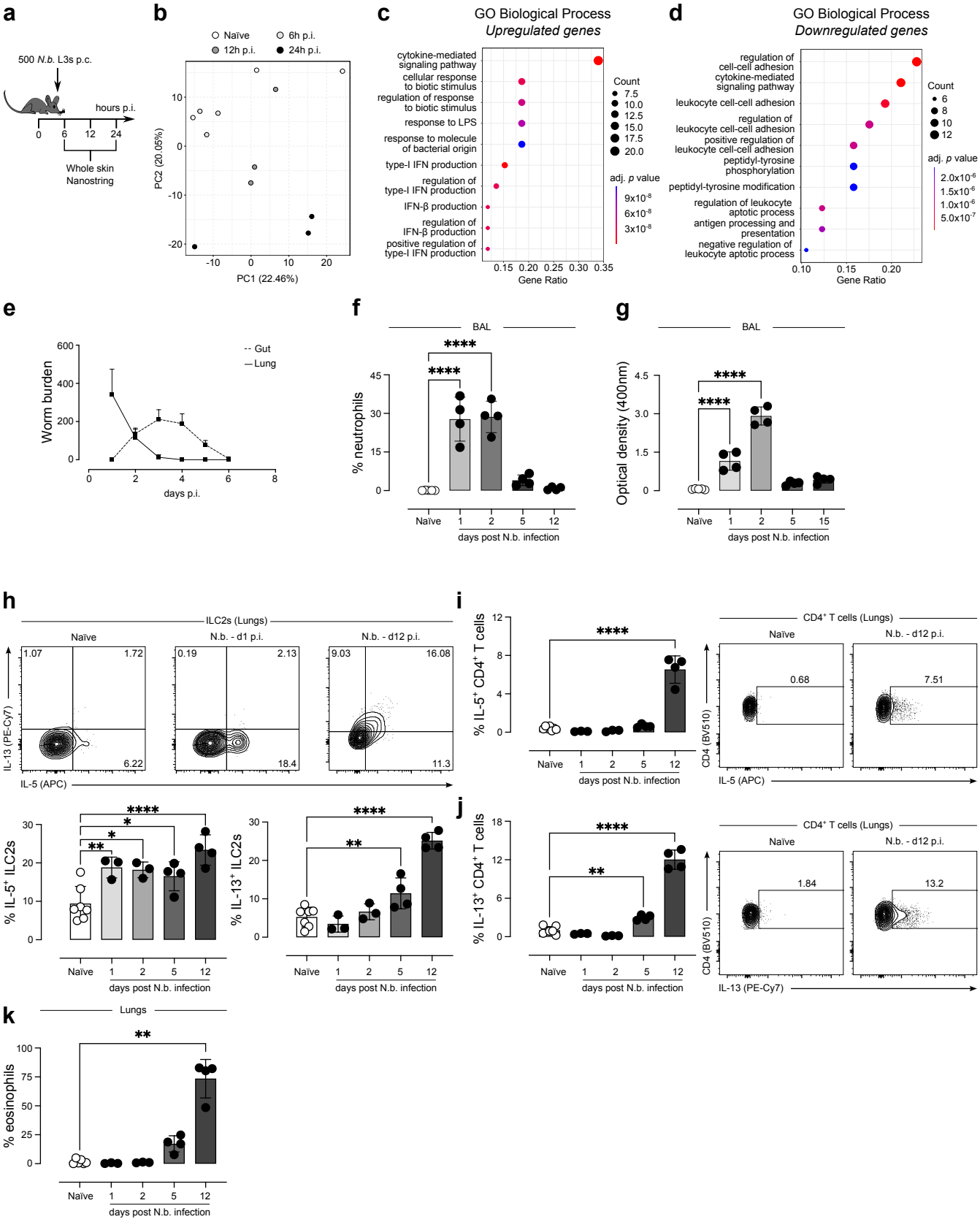

Extended Data Fig. 1 *(previous page). N. brasiliensis* p.c. infection recapitulates the hallmarks of the s.c. route of infection. **a**, Worm burden measured in the lungs (dashed line) and small intestines (full line) of mice infected s.c. with 500 *N. brasiliensis* L3s throughout time. **b**, Mice were infected with 500 L3s as described in Fig. 1a and ears were collected at 6h, 12h and 24h p.i. for subsequent NanoString analysis. **c**, Skin RNA from naïve (white circles), and *N. brasiliensis*-infected (light grey to black) C57BL/6J mice was analysed with the Mouse Host Response V1 NanoString panel and total sample variation was summarised via principal component analysis (PCA) across all genes. (n = 3 mice per group). **d, e**, Overrepresented GO: biological processes in upregulated (d) and downregulates (e) DEGs from *N. brasiliensis*-infected at 24h p.i. **f,g**, Frequencies of neutrophils within total leukocytes (**f**), and optical density (measured at 400nm) (**g**) in the BAL throughout the course of *N. brasiliensis* s.c. infection (500 *N. brasiliensis* L3s; n = 4-5 mice per group). **h**, Flow cytometry analysis of intracellular IL-5 and IL-13 in ILC2s isolated from the lungs of naïve and *N. brasiliensis*-infected C57BL/6J mice and stimulated *ex vivo* for 4h. Summary graph showing the percentages of IL-5$^+$ and IL-13$^+$ cells within the ILC2 population (n = 3-7 mice per group). **i,j**, Flow cytometry analysis and summary graphs of intracellular IL-5 (i) and IL-13 (j) in CD4$^+$ T cells isolated from the lungs of naïve and *N. brasiliensis*-infected C57BL/6J mice and stimulated *ex vivo* for 4h (n = 3-7 mice per group). **k**, Frequencies of eosinophils within total leukocytes in the BAL throughout the course of *N. brasiliensis* p.c. infection (n = 3-6 mice per group). **f-k**, Error bars represent mean±SD. Normality of the samples was assessed with Shapiro-Wilk normality test; statistical analysis was then performed using Kruskal-Wallis or one-way ANOVA test. * $p < 0.05$; ** $p < 0.01$; **** $p < 0.0001$

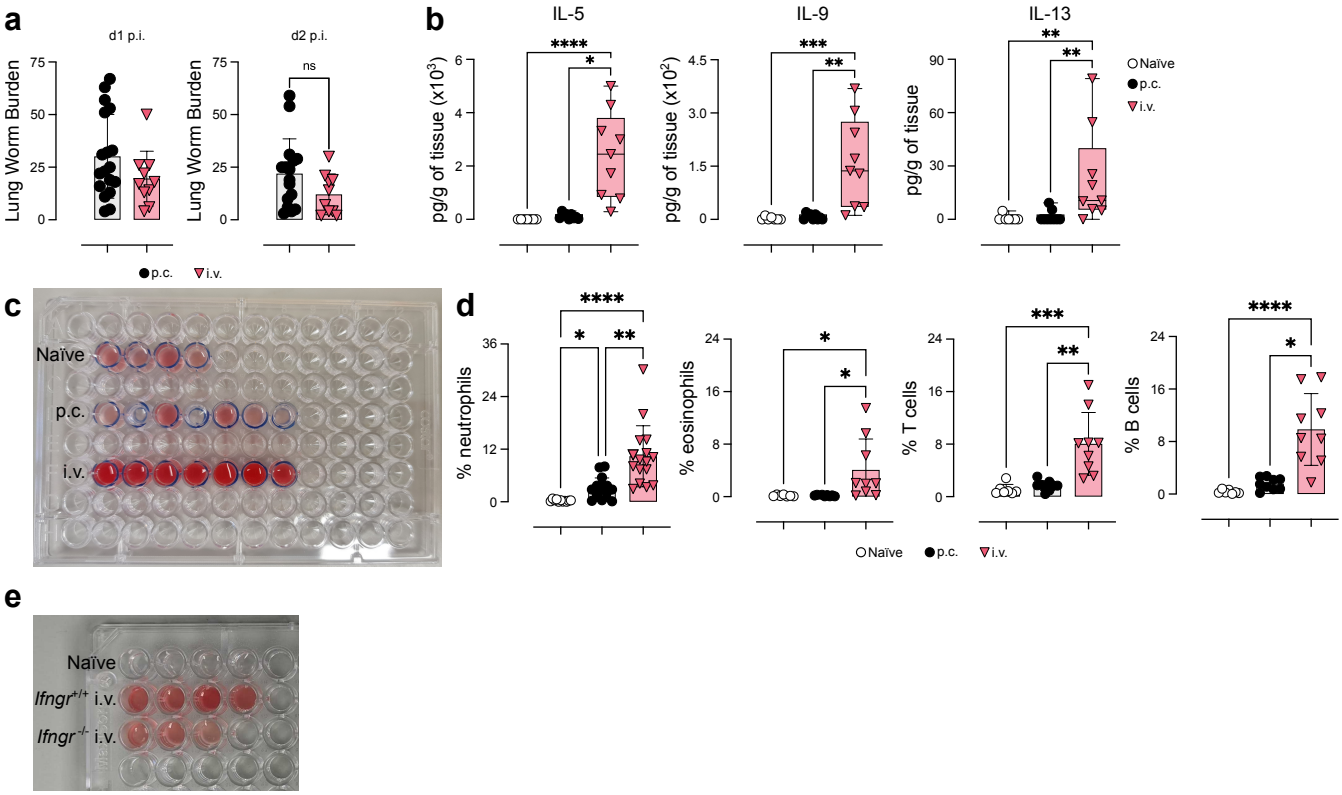

Extended Data Fig. 2. Bypassing the skin phase of infection precludes the induction of lung type-17 responses and results in increased IFN-γ-dependent lung bleeding during *N. brasiliensis* larvae migration. **a**, Worm burden measured in the lungs of mice infected p.c. with 500 *N. brasiliensis* L3s (black circles) and i.v. with with 200 *N. brasiliensis* L3s (pink triangles), at days 1 and 2 p.i.. **b**, Cytokine levels in total lung tissue from naïve (white circles), p.c. (black circles) and i.v. (pink triangles) *N. brasiliensis*-infected C57BL/6J mice normalised by 1 gram of tissue, measured by LEGENDPlex™ (n = 7-9 mice per group; pool of 2 independent experiments). **c**, Representative picture of the measurements shown in Fig. 2g (n = 4-7 mice per group). **d**, Frequencies of neutrophils, eosinophils, T cells and B cells within total leukocytes in the lungs of naïve (white circles), p.c. (black circles) and i.v. (pink triangles) *N. brasiliensis*-infected C57BL/6J mice at day 1 p.i. (n = 7-9 mice per group; pool of 2 independent experiments). **e**, Representative picture of the measurements shown in Fig. 2j (n = 3-4 mice per group). **a, d**, Error bars represent mean±SD. b, Box-and-whisker plots display first and third quartiles, and the median; whiskers are from each quartile to the minimum or maximum. **a, b, d**. Normality of the samples was assessed with Shapiro-Wilk normality test and statistical analysis was then performed accordingly. * $p < 0.05$; ** $p < 0.01$; *** $p < 0.001$; **** $p < 0.0001$

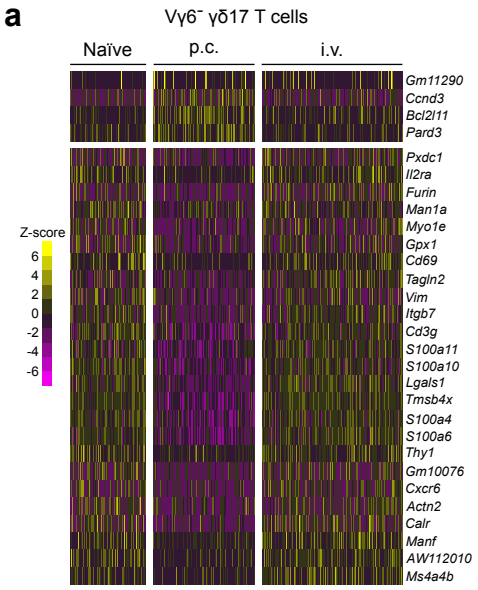

Extended Data Fig. 3. P.c., but not i.v., *N. brasiliensis* infection induces the activation of Vγ6⁺ γδ17 T cells and suppression of IFN-γ-producing innate lymphocytes. **a**, Heatmap showing the DEGs in Vγ6⁻ γδ17 T cells from naïve, p.c.- and i.v.-infected animals. Scale represents scaled and centred z-scores. scRNAseq data consists of sorted cells pooled from 4 mice per group.

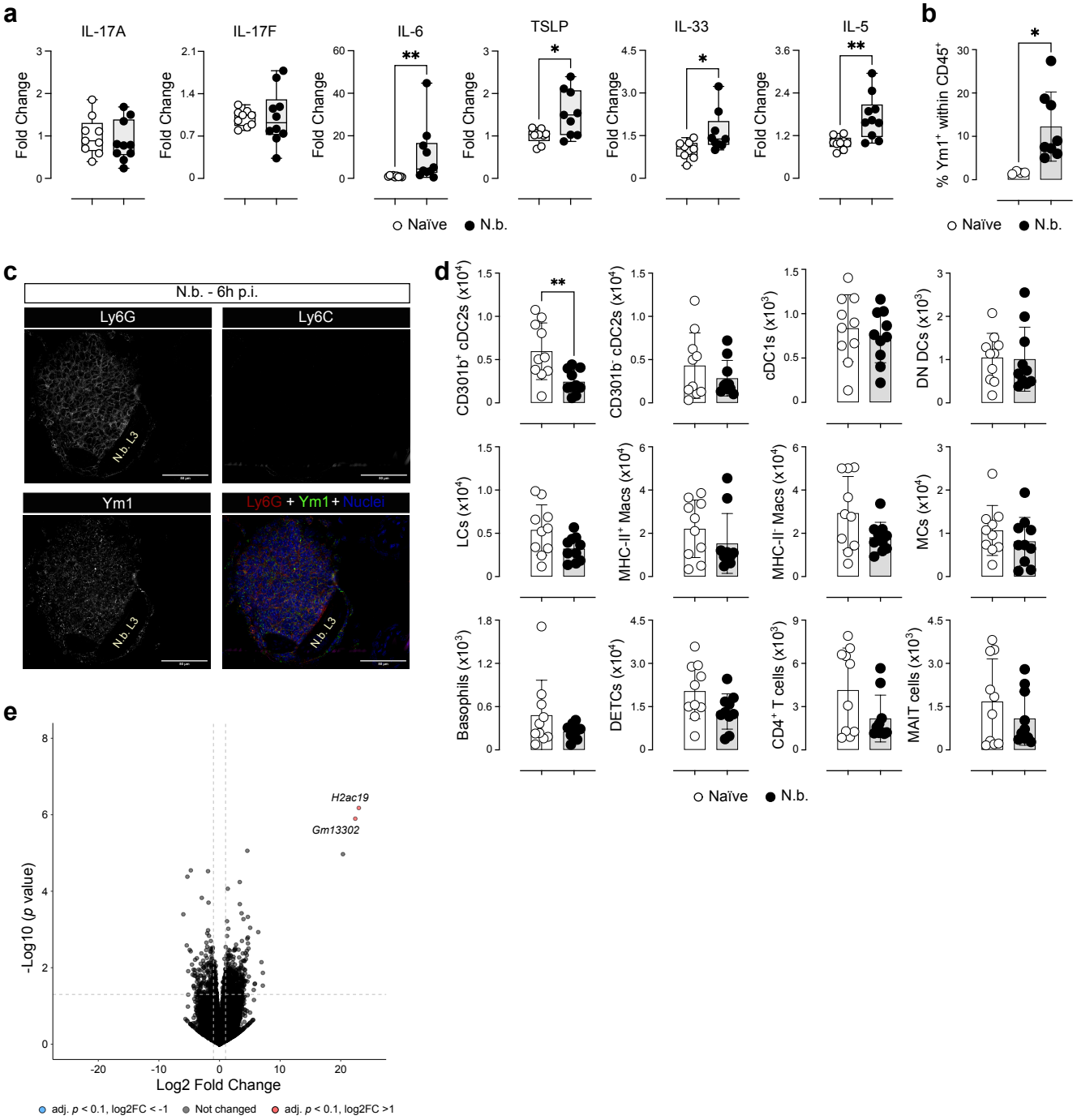

Extended Data Fig. 4. *N. brasiliensis* larvae induce a migratory transcriptional program in dermal γδ T cells. **a**, Cytokine levels in total skin tissue from naïve (white circles), and *N. brasiliensis*-infected (black circles) C57BL/6J mice measured by LEGENDPlex™ and displayed as fold change in relation to the average of the naïve group (n = 9-10 mice per group; pool of 2 independent experiments). **b**, Summary graph from the flow cytometry analysis of intracellular Ym1 in total leukocytes isolated from the skin of naïve (white circles) and *N. brasiliensis*-infected (black circles) mice (n = 4-8 mice per group; pool of 2 independent experiments). **c**, Immunofluorescence of *N. brasiliensis* larvae and recruited immune cells in the skin of C57BL/6J mice at 6h p.i. d, Summary graphs showing the numbers of skin immune cell populations from naïve (white circles) and *N. brasiliensis*-infected (black circles) mice at 24h p.i. (n = 9-10 mice per group; pool of 2 independent experiments). **e**, DEGs from DETCs were visualised using a volcano plot, genes significantly upregulated (red), and downregulated (blue) during *N. brasiliensis* infection were defined as having an adjusted *p* value of <0.1 and absolute log2 fold change of >1. a, Box-and-whisker plots display first and third quartiles, and the median; whiskers are from each quartile to the minimum or maximum. **b,d**, Error bars represent mean±SD. **a, b, d**. Normality of the samples was assessed with Shapiro-Wilk normality test and statistical analysis was then performed accordingly. * $p < 0.05$; ** $p < 0.01$.

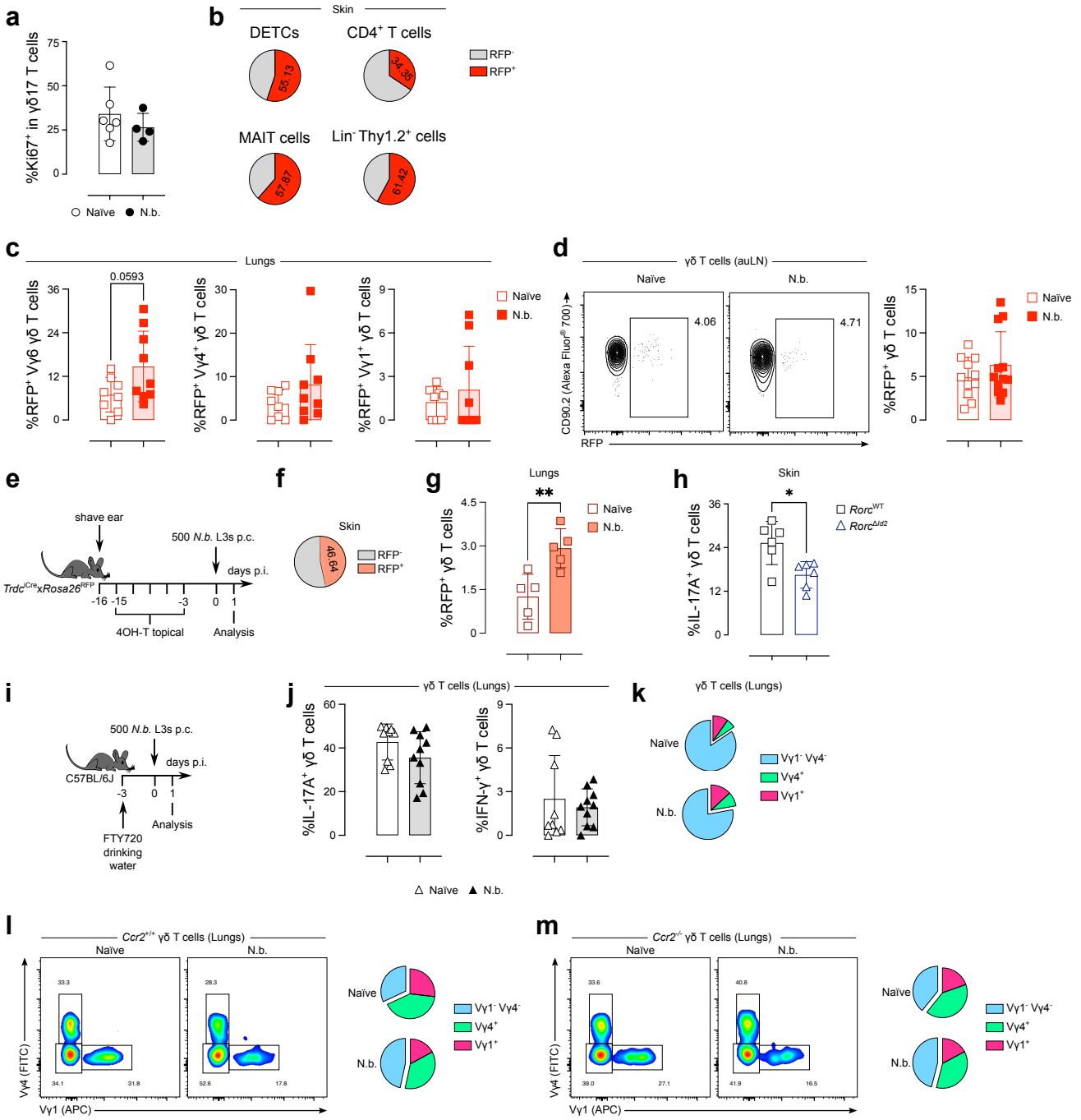

Extended Data Fig. 5. Migratory dermal γδ17 T cells are responsible for the expansion in the lung γδ17 T cell population during *N. brasiliensis* infection. **a**, Summary graph from the flow cytometry analysis of intracellular Ki67 in γδ17 T cells isolated from the lungs of naïve (white circles) and *N. brasiliensis*-infected (black circles) mice (n = 4-6 mice per group). **b**, Summary pie charts showing the percentage of RFP$^+$ cells (red slice) within DETCs, CD4$^+$ T cells, MAIT cells and Lin-Thy1.2$^+$ cells in naïve *Id2*^{CreERT2}x*Rosa26*^{RFP} mice (n = 11-13 mice). **c**, Summary graphs showing the percentages of RFP$^+$ cells within Vγ1$^-$Vγ4$^-$, Vγ1$^-$Vγ4$^+$ and Vγ1$^+$Vγ4$^-$ γδ T cells isolated from the lungs of naïve (white squares) and *N. brasiliensis*-infected (red squares) *Id2*^{CreERT2}x*Rosa26*^{RFP} mice (n = 8-9 mice per group; pool of 3 independent experiments). **d**, Flow cytometry analysis of RFP expression and summary graph showing the percentage of RFP$^+$ cells within total γδ T cells isolated from the ear-draining lymph nodes of naïve (white squares) and *N. brasiliensis*-infected (red squares) *Id2*^{CreERT2}x*Rosa26*^{RFP} mice (n = 11-12 mice per group; pool of 3 independent experiments). **e**, *Trdc*^{CreERT2}x*Rosa26*^{RFP} mice had their right ear shaved, and starting on the following day were treated for five times with 4OH-T over the course of two weeks. Mice were then rested for 3 days before being infected with 500 *N. brasiliensis* L3s p.c. **f**, Summary pie charts showing the percentage of RFP$^+$ cells (orange slice) within dermal γδ T cells in the skin of naïve *Trdc*^{CreERT2}x*Rosa26*^{RFP} mice (n = 10). **g**, Summary graph showing the percentages of RFP$^+$ cells within γδ T cells isolated from the lungs of naïve (white squares) and *N. brasiliensis*-infected (orange squares) *Trdc*^{CreERT2}x*Rosa26*^{RFP} mice (n = 5 mice per group). **h**, Summary graph showing the percentages of IL-17A$^+$ cells within the dermal γδ T cell population isolated from the skin of naïve (white squares) and *N. brasiliensis*-infected (white triangles) *Id2*^{CreERT2}x*Rorc*$^{fl/fl}$ mice (n = 5-6 mice per group). **i**, C57BL/6J mice were treated with FTY720 in the drinking water starting 3 days prior to the infection, and were then infected or not with 500 *N. brasiliensis* L3s p.c.; mice were analysed at day 1 p.i. **j**, Summary graphs showing the percentages of IL-17A$^+$ and IFN-γ$^+$ cells within lung γδ T cells from FTY720-treated naïve (white triangles) and *N. brasiliensis*-infected (black triangles) mice after 4h of *ex vivo* stimulation (n = 9-10 mice per group; pool of 2 independent experiments). **k**, Summary pie charts showing the Vγ usage in total lung γδ T cells from FTY720-treated naïve (top) and *N. brasiliensis*-infected (bottom) mice (n = 9-10 mice per group; pool of 2 independent experiments). **l, m**, Flow cytometry analysis and summary pie charts showing the Vγ usage in total lung γδ T cells from *Ccr2*$^{+/+}$ (**l**) and *Ccr2*$^{-/-}$ (**m**) mice (n = 6-10 mice per group; pool of 3 independent experiments). **a-j**, Error bars represent mean±SD. Normality of the samples was assessed with Shapiro-Wilk normality test and statistical analysis was then performed accordingly. * $p < 0.05$.

Extended Data Table 1

Type-1 effector genes
Ifng
Gzmb
Gzma
Cd7
Tbx21
Ccl5
Klrc2
Ly6c2
Nkg7
Klrd1
Ctsw
Cd2
Cd27
Klre1
Xcl1
Lck
Cd28
Tyrobp
Sell
Fasl
Ncr1
Il2rb
Fcer1g
Itgb2
Prf1
Slamf7
Runx3
Lgals1

Extended Data Table 2

ENSEMBL	baseMean	log2FoldChange	lfcSE	stat	pvalue	padj	SYMBOL
ENSMUSG00000005413	134.7077323	1.000906093	0.360166957	2.7790059	0.005453	0.08	Hmox1
ENSMUSG00000056917	298.0656223	1.005444458	0.334637044	3.0045821	0.002659	0.08	Sipa1
ENSMUSG00000006019	149.1124369	1.014081629	0.305020372	3.3246357	8.85E-04	0.08	Dhx34
ENSMUSG00000027630	351.0492915	1.023091324	0.262532331	3.8970108	9.74E-05	0.03	Tbl1xr1
ENSMUSG00000039450	180.66718	1.027292766	0.340538107	3.0166749	0.002556	0.08	Dcxr
ENSMUSG00000046791	229.7740329	1.028560118	0.328611062	3.1300228	0.001748	0.08	Riox1
ENSMUSG00000034336	123.7363184	1.030045376	0.348130653	2.9587897	0.003088	0.08	Ina
ENSMUSG00000025351	201.1280755	1.03091046	0.343338901	3.0026031	0.002677	0.08	Cd63
ENSMUSG00000049892	235.9294529	1.039730346	0.346247265	3.002855	0.002675	0.08	Rasd1
ENSMUSG00000042854	135.1739836	1.040617161	0.274847247	3.7861655	1.53E-04	0.04	Trp53rkb
ENSMUSG00000091956	300.4901895	1.042048645	0.446423401	2.334216	0.019584	0.09	C2cd4b
ENSMUSG00000021036	702.386515	1.043690193	0.237361465	4.3970498	1.10E-05	0.01	Sptlc2
ENSMUSG00000003068	562.7181566	1.048190886	0.316996684	3.3066304	9.44E-04	0.08	Stk11
ENSMUSG00000044348	108.2972254	1.049035879	0.300344948	3.4927702	4.78E-04	0.07	Slc25a53
ENSMUSG00000030741	368.0622069	1.049377215	0.307853841	3.4086865	6.53E-04	0.07	Spns1
ENSMUSG00000015396	419.5702322	1.051882419	0.275259111	3.8214263	1.33E-04	0.04	Cd83
ENSMUSG00000020253	194.9391997	1.056348875	0.383712987	2.7529662	0.005906	0.08	Ppm1m
ENSMUSG00000041481	1037.925337	1.065738265	0.35528383	2.9996813	0.002703	0.08	Serpina3g
ENSMUSG00000006378	248.4985824	1.066308142	0.362639107	2.9404113	0.003278	0.08	Gcat
ENSMUSG00000021765	119.6144144	1.066998869	0.435157361	2.451984	0.014207	0.08	Fst
ENSMUSG00000020235	753.79355	1.075008841	0.334226894	3.2164044	0.001298	0.08	Fzr1
ENSMUSG00000019773	98.84825544	1.075072221	0.360165265	2.9849414	0.002836	0.08	Fbxo5
ENSMUSG00000030104	1169.946889	1.076031957	0.288493009	3.7298372	1.92E-04	0.05	Edem1
ENSMUSG00000037531	115.8018734	1.079914834	0.311942397	3.4619046	5.36E-04	0.07	Mrpl47
ENSMUSG00000024382	197.3040077	1.086017602	0.306794883	3.5398817	4.00E-04	0.06	Ercc3
ENSMUSG00000020592	518.9584971	1.086136887	0.261653524	4.1510501	3.31E-05	0.02	Sdc1
ENSMUSG00000098923	373.6305095	1.087202339	0.30143914	3.6067059	3.10E-04	0.06	Tmem185b
ENSMUSG00000061353	214.9682295	1.087399126	0.361222222	3.0103329	0.00261	0.08	Cxcl12
ENSMUSG00000024906	168.0253477	1.087410536	0.295405256	3.6810805	2.32E-04	0.06	Mus81
ENSMUSG00000019960	433.8300501	1.100719222	0.282859665	3.8913969	9.97E-05	0.03	Dusp6
ENSMUSG00000071757	113.4554389	1.103598124	0.355661977	3.102941	0.001916	0.08	Zhx2
ENSMUSG00000015747	250.9701473	1.10541154	0.330242514	3.3472721	8.16E-04	0.08	Vps45
ENSMUSG00000031403	708.6433779	1.110511317	0.228127435	4.8679429	1.13E-06	0	Dkc1
ENSMUSG00000041684	161.9001721	1.129400486	0.416786224	2.7097836	0.006733	0.08	Bivm
ENSMUSG00000068580	151.8278132	1.132343769	0.284304625	3.9828538	6.81E-05	0.03	Zfyve19
ENSMUSG00000006398	221.0996773	1.133400169	0.340366466	3.3299408	8.69E-04	0.08	Cdc20
ENSMUSG00000008136	126.3105047	1.141032692	0.353016321	3.2322378	0.001228	0.08	Fhl2
ENSMUSG00000094525	116.658259	1.16466089	0.329279325	3.5369997	4.05E-04	0.06	Trbv12-2
ENSMUSG00000031242	96.83115584	1.177311093	0.352369405	3.3411275	8.34E-04	0.08	2610002M06Rik
ENSMUSG00000046550	116.5272353	1.199793264	0.394238018	3.0433221	0.00234	0.08	Spin2c
ENSMUSG00000039810	297.6677396	1.209272466	0.329391333	3.6712334	2.41E-04	0.06	Zc3h10

ENSMUSG00000022550	184.9243097	1.2155018	0.322431366	3.7698001	1.63E-04	0.04	Adck5
ENSMUSG00000029073	158.7162293	1.238812621	0.387716706	3.1951489	0.001398	0.08	Cptp
ENSMUSG00000024742	396.541404	1.250268126	0.3884059	3.2189731	0.001287	0.08	Fen1
ENSMUSG00000047515	97.04465476	1.266071075	0.422088459	2.9995397	0.002704	0.08	BC049715
ENSMUSG00000037816	173.0512555	1.277108939	0.310643104	4.1111775	3.94E-05	0.02	Fbxw17
ENSMUSG00000025962	158.7378883	1.32855035	0.268352196	4.9507713	7.39E-07	0	Fastkd2
ENSMUSG00000028270	110.5688572	1.343901016	0.324984962	4.1352714	3.55E-05	0.02	Gbp2
ENSMUSG00000064267	136.0783255	1.400336385	0.441653851	3.170665	0.001521	0.08	Hvcn1
ENSMUSG00000079018	98.12705297	1.427676868	0.428575994	3.3312105	8.65E-04	0.08	Ly6c1
ENSMUSG00000095562	284.168869	1.48365967	0.308104859	4.8154374	1.47E-06	0	Erdr1
ENSMUSG00000038002	133.0969695	1.497652202	0.334739557	4.4740819	7.67E-06	0.01	Cramp1
ENSMUSG00000096768	1668.262146	1.574503162	0.307542755	5.1196237	3.06E-07	0	Erdr1
ENSMUSG00000026879	2194.829649	1.677330335	0.295945048	5.6677087	1.45E-08	0	Gsn
ENSMUSG00000074695	167.8447178	1.885355882	0.379737123	4.9648975	6.87E-07	0	Il22
ENSMUSG00000025492	225.0765122	1.933533801	0.665682346	2.9045893	0.003677	0.08	Ifitm3
ENSMUSG00000000753	111.0346326	1.944839507	0.486545107	3.997244	6.41E-05	0.03	Serpinf1
ENSMUSG00000043613	105.7964433	2.015289851	0.81128252	2.484079	0.012989	0.08	Mmp3
ENSMUSG00000041378	211.307185	2.467665308	0.483403937	5.1047687	3.31E-07	0	Cldn5
ENSMUSG00000064201	818.2737389	2.485597623	1.080861791	2.2996443	0.021468	0.09	Krt2
ENSMUSG00000025746	221.528025	2.510021697	0.713377537	3.518504	4.34E-04	0.06	Il6
ENSMUSG00000018593	1388.692513	2.658925162	0.313162217	8.4905682	2.06E-17	0	Sparc
ENSMUSG00000019929	469.9003005	2.9585274	0.610897451	4.8429199	1.28E-06	0	Dcn
ENSMUSG00000035385	138.1477681	3.100932053	0.945049655	3.2812372	0.001034	0.08	Ccl2
ENSMUSG00000022650	132.868814	-4.242518493	1.073172029	-3.9532511	7.71E-05	0.03	Retnlb
ENSMUSG00000037712	8947.347622	-2.97844122	0.774303863	-3.8466051	1.20E-04	0.04	Fermt2
ENSMUSG00000079598	233.8601589	-2.927604238	1.027977726	-2.8479258	0.004401	0.08	Clec2l
ENSMUSG00000018341	4035.366844	-2.850440165	0.929397515	-3.0669763	0.002162	0.08	Il12rb2
ENSMUSG00000057729	149.1006117	-2.84238761	0.958582222	-2.9651996	0.003025	0.08	Prtn3
ENSMUSG00000028359	844.4980445	-2.710649993	0.759577292	-3.5686296	3.59E-04	0.06	Orm3
ENSMUSG00000117495	154.040501	-2.604233389	1.0728631	-2.4273678	0.015209	0.09	Gm4125
ENSMUSG00000051855	18713.88854	-2.580070406	0.841808931	-3.0649121	0.002177	0.08	Mest
ENSMUSG00000031424	2197.305437	-2.514240267	0.8071556	-3.1149388	0.00184	0.08	Kir3dl1
ENSMUSG00000055485	333.8134922	-2.45141593	0.46794965	-5.2386318	1.62E-07	0	Soga1
ENSMUSG00000004612	50230.35963	-2.416502608	0.870308688	-2.776604	0.005493	0.08	Nkg7
ENSMUSG00000040229	1965.653843	-2.407089355	0.694357312	-3.4666436	5.27E-04	0.07	Gpr34
ENSMUSG00000039037	152.6018345	-2.40409949	0.952802869	-2.5231867	0.01163	0.08	St6galnac5
ENSMUSG00000032380	4312.010386	-2.396616714	0.681031875	-3.5190962	4.33E-04	0.06	Dapk2
ENSMUSG00000058715	17722.20844	-2.387307882	0.867138164	-2.7530882	0.005904	0.08	Fcer1g
ENSMUSG00000030775	22055.59935	-2.38062121	0.769452033	-3.0939176	0.001975	0.08	Trat1
ENSMUSG00000018470	598.4618344	-2.370183667	0.74371155	-3.1869663	0.001438	0.08	Kcnab3
ENSMUSG00000042638	2843.909366	-2.344538491	0.728171986	-3.2197593	0.001283	0.08	Gucy2c
ENSMUSG00000068246	205.4435101	-2.323641852	0.493333742	-4.7100809	2.48E-06	0	Apol9b
ENSMUSG00000057439	1817.050068	-2.314696521	0.852804977	-2.7142155	0.006643	0.08	Kir3dl2
ENSMUSG00000032554	30619.75901	-2.223551514	0.829272147	-2.6813291	0.007333	0.08	Trf
ENSMUSG00000030283	1289.688132	-2.217381962	0.914600523	-2.4244267	0.015333	0.09	St8sia1

ENSMUSG00000079445	159.4759802	-2.215221233	0.775424634	-2.8567847	0.00428	0.08	B3gnt7
ENSMUSG00000015950	1577.848358	-2.21504393	0.716183843	-3.0928426	0.001982	0.08	Ncf1
ENSMUSG00000023031	6949.689931	-2.209221782	0.733721231	-3.0109825	0.002604	0.08	Cela1
ENSMUSG00000020811	718.4048009	-2.204192694	0.714979882	-3.0828737	0.00205	0.08	Wscd1
ENSMUSG00000024664	1146.95277	-2.165201403	0.766561006	-2.824565	0.004734	0.08	Fads3
ENSMUSG00000032369	6474.609914	-2.051192532	0.903636233	-2.2699317	0.023212	0.09	Plscr1
ENSMUSG00000000409	7847.903639	-1.967858453	0.708736515	-2.7765727	0.005494	0.08	Lck
ENSMUSG00000029821	3833.106884	-1.921036293	0.592172658	-3.2440476	0.001178	0.08	Gsdme
ENSMUSG00000070469	531.5735359	-1.902910083	0.444367673	-4.2822874	1.85E-05	0.01	Adamtsl3
ENSMUSG00000035273	698.2614784	-1.899234093	0.659005831	-2.8819686	0.003952	0.08	Hpse
ENSMUSG00000026576	2209.906678	-1.889847776	0.613741219	-3.0792258	0.002075	0.08	Atp1b1
ENSMUSG00000004933	5244.769024	-1.884904295	0.780931358	-2.4136619	0.015793	0.09	Matk
ENSMUSG00000020793	229.5652367	-1.882314984	0.728036882	-2.5854665	0.009725	0.08	Galr2
ENSMUSG00000018217	4459.715866	-1.8765222	0.680081647	-2.7592602	0.005793	0.08	Pmp22
ENSMUSG00000037202	2267.699319	-1.823019851	0.621777153	-2.9319505	0.003368	0.08	Prf1
ENSMUSG00000025163	42659.57281	-1.822534152	0.680676591	-2.6775332	0.007417	0.08	Cd7
ENSMUSG00000034528	733.4033397	-1.779338151	0.721422782	-2.4664291	0.013647	0.08	Hsd17b13
ENSMUSG00000074874	10953.52542	-1.774271458	0.722424241	-2.4559966	0.014049	0.08	Ctla2b
ENSMUSG00000045672	2304.667143	-1.753326454	0.413252423	-4.2427494	2.21E-05	0.01	Col27a1
ENSMUSG00000028601	1642.741955	-1.746239447	0.658611006	-2.6513973	0.008016	0.08	Echdc2
ENSMUSG00000116975	663.4118634	-1.727089152	0.648827757	-2.6618608	0.007771	0.08	4930470H14Rik
ENSMUSG00000021662	357.7797611	-1.724801646	0.477659932	-3.6109406	3.05E-04	0.06	Arhgef28
ENSMUSG00000026357	201.0386936	-1.689105983	0.729943158	-2.314024	0.020666	0.09	Rgs18
ENSMUSG00000028041	1048.594386	-1.671800524	0.403412612	-4.1441454	3.41E-05	0.02	Adam15
ENSMUSG00000020399	2048.845533	-1.66004595	0.608331005	-2.7288531	0.006356	0.08	Havcr2
ENSMUSG00000030173	222.949446	-1.656673407	0.528438962	-3.1350327	0.001718	0.08	Klra5
ENSMUSG00000030516	229.105224	-1.645914239	0.373935595	-4.4015982	1.07E-05	0.01	Tjp1
ENSMUSG00000030410	213.7099729	-1.643649106	0.714245583	-2.301238	0.021378	0.09	Dmwd
ENSMUSG00000032782	1279.804908	-1.640574686	0.584846799	-2.8051358	0.00503	0.08	Cntrob
ENSMUSG00000030352	374.9190525	-1.629613435	0.416288099	-3.9146289	9.05E-05	0.03	Tspan9
ENSMUSG00000024986	513.1789702	-1.614373263	0.425576083	-3.7933834	1.49E-04	0.04	Hhex
ENSMUSG00000051359	597.8410473	-1.611875375	0.461234036	-3.4947017	4.75E-04	0.07	Ncald
ENSMUSG00000028358	96.75196129	-1.611310902	0.698804418	-2.305811	0.021121	0.09	Zfp618
ENSMUSG00000030854	676.456163	-1.594582347	0.373825003	-4.2655851	1.99E-05	0.01	Ptpn5
ENSMUSG00000023033	1033.268647	-1.591498646	0.404903348	-3.9305643	8.47E-05	0.03	Scn8a
ENSMUSG00000004709	2380.049768	-1.574855503	0.410083193	-3.8403317	1.23E-04	0.04	Cd244a
ENSMUSG00000075046	110.1776889	-1.55472752	0.487122164	-3.1916583	0.001415	0.08	Duxf3
ENSMUSG00000070348	1332.330033	-1.540923972	0.42767042	-3.6030642	3.14E-04	0.06	Ccnd1
ENSMUSG00000040016	354.1673283	-1.523598888	0.46112205	-3.304112	9.53E-04	0.08	Ptger3
ENSMUSG00000038843	2297.241737	-1.498288492	0.608857484	-2.4608197	0.013862	0.08	Gcnt1
ENSMUSG00000021271	1061.13061	-1.486035903	0.385298102	-3.8568472	1.15E-04	0.04	Zfp839
ENSMUSG00000058806	121.0261089	-1.471284231	0.452729828	-3.2498063	0.001155	0.08	Col13a1
ENSMUSG00000029919	867.9220981	-1.458967604	0.443941343	-3.2863972	0.001015	0.08	Hpgds
ENSMUSG00000093979	453.5900926	-1.458262482	0.630811688	-2.3117239	0.020793	0.09	Gm2237

ENSMUSG00000022469	365.7784061	-1.442433028	0.418437908	-3.4471854	5.66E-04	0.07	Rapgef3
ENSMUSG00000021806	224.446036	-1.393290324	0.35886498	-3.8824917	1.03E-04	0.03	Nid2
ENSMUSG00000053101	308.6630985	-1.359049805	0.440236257	-3.0870919	0.002021	0.08	Gpr141
ENSMUSG00000042320	880.8071983	-1.334487562	0.438762703	-3.041479	0.002354	0.08	Prox2
ENSMUSG00000039976	113.9911667	-1.32034059	0.512917379	-2.5741779	0.010048	0.08	Tbc1d16
ENSMUSG00000039960	395.2872139	-1.314345959	0.427241199	-3.0763558	0.002095	0.08	Rhou
ENSMUSG00000038304	1561.894332	-1.301514139	0.428710486	-3.0358813	0.002398	0.08	Cd160
ENSMUSG00000052336	555.7677568	-1.301242604	0.371332848	-3.5042486	4.58E-04	0.07	Cx3cr1
ENSMUSG00000050910	154.3980969	-1.298797932	0.444063417	-2.9248028	0.003447	0.08	Cdr2l
ENSMUSG00000025856	210.4580273	-1.298425801	0.493487796	-2.6311204	0.00851	0.08	Pdgfa
ENSMUSG00000000303	595.2943187	-1.283205983	0.426290338	-3.0101691	0.002611	0.08	Cdh1
ENSMUSG00000034653	331.9106571	-1.26510211	0.433115962	-2.9209316	0.00349	0.08	Ythdc2
ENSMUSG00000049109	309.1840465	-1.264863014	0.381331171	-3.3169673	9.10E-04	0.08	Themis
ENSMUSG00000097011	124.5465204	-1.239389156	0.463062749	-2.6765037	0.007439	0.08	Gm4651
ENSMUSG00000040312	408.8657379	-1.225141246	0.388733896	-3.1516193	0.001624	0.08	Cchcr1
ENSMUSG00000039963	108.6522014	-1.221139694	0.5078309	-2.4046187	0.016189	0.09	Ccdc40
ENSMUSG00000029406	520.6183281	-1.217809038	0.345958739	-3.5200991	4.31E-04	0.06	Pitpnm2
ENSMUSG00000042647	333.0194117	-1.203218461	0.375358201	-3.2055206	0.001348	0.08	Acad12
ENSMUSG00000064084	444.0436767	-1.201008927	0.387699548	-3.0977826	0.00195	0.08	Olfr1202
ENSMUSG00000027860	264.0611627	-1.191757367	0.337460126	-3.5315502	4.13E-04	0.06	Vangl1
ENSMUSG00000048186	226.2538188	-1.187652154	0.498736103	-2.3813238	0.017251	0.09	Bend7
ENSMUSG00000050271	455.9814761	-1.186526559	0.426829977	-2.7798576	0.005438	0.08	Prag1
ENSMUSG00000015133	329.466244	-1.158186591	0.26635087	-4.3483492	1.37E-05	0.01	Lrrk1
ENSMUSG00000021097	127.8880344	-1.154209047	0.476483571	-2.422348	0.015421	0.09	Clmn
ENSMUSG00000029638	985.9174938	-1.149907241	0.449940866	-2.5556853	0.010598	0.08	Glcci1
ENSMUSG00000028184	894.3551851	-1.149165631	0.324978348	-3.5361298	4.06E-04	0.06	Adgrl2
ENSMUSG00000026556	151.9549479	-1.140275196	0.377048226	-3.0242158	0.002493	0.08	Vangl2
ENSMUSG00000029521	3088.021255	-1.123823411	0.433868762	-2.5902381	0.009591	0.08	Chek2
ENSMUSG00000020185	184.5768974	-1.120095123	0.452456825	-2.4755845	0.013302	0.08	E2f7
ENSMUSG00000044550	405.5984175	-1.106989979	0.431170808	-2.5674047	0.010246	0.08	Tceal3
ENSMUSG00000031565	170.2155595	-1.105947472	0.334902623	-3.3022956	0.000959	0.08	Fgfr1
ENSMUSG00000037617	506.2835131	-1.102872675	0.370249382	-2.9787293	0.002894	0.08	Spag1
ENSMUSG00000032443	208.7635467	-1.089234409	0.302869959	-3.5963765	3.23E-04	0.06	Zcwpw2
ENSMUSG00000051934	177.4268613	-1.084301969	0.295588372	-3.6682836	2.44E-04	0.06	Spats2
ENSMUSG00000018849	2060.580058	-1.084284325	0.333628305	-3.249977	0.001154	0.08	Wwc1
ENSMUSG00000060470	1468.479285	-1.080200959	0.416145928	-2.5957264	0.009439	0.08	Adgrg3
ENSMUSG00000037492	689.1942458	-1.078090931	0.391399047	-2.7544547	0.005879	0.08	Zmat4
ENSMUSG00000024665	329.3649286	-1.072930831	0.346405536	-3.0973259	0.001953	0.08	Fads2
ENSMUSG00000046873	972.6979662	-1.070005401	0.369742392	-2.8939213	0.003805	0.08	Mbtps2
ENSMUSG00000055322	823.6684364	-1.06551072	0.325568894	-3.2727657	0.001065	0.08	Tns1
ENSMUSG00000029564	106.0576344	-1.065120357	0.36327275	-2.9320128	0.003368	0.08	4930519G04Rik
ENSMUSG00000052584	442.640584	-1.062601078	0.452944107	-2.3459872	0.018977	0.09	Serp2
ENSMUSG00000023267	345.5572793	-1.059865276	0.442792719	-2.3935924	0.016684	0.09	Gabrr2
ENSMUSG00000038473	219.7662286	-1.054736306	0.341565288	-3.0879493	0.002015	0.08	Nos1ap

ENSMUSG00000039086	849.6750341	-1.0535866	0.431521118	-2.4415644	0.014624	0.09	Ss18l1
ENSMUSG00000023011	145.1210228	-1.043250598	0.415583009	-2.5103303	0.012062	0.08	Faim2
ENSMUSG00000000562	822.0449468	-1.041973959	0.413389416	-2.5205627	0.011717	0.08	Adora3
ENSMUSG00000023008	529.9866859	-1.039001964	0.444809724	-2.3358346	0.0195	0.09	Fmnl3
ENSMUSG00000002059	575.4283632	-1.035779262	0.389174411	-2.6614783	0.00778	0.08	Rab34
ENSMUSG00000026018	321.0060486	-1.030284729	0.402139542	-2.562008	0.010407	0.08	Ica1l
ENSMUSG00000090799	190.1866491	-1.02970576	0.383051532	-2.6881651	0.007185	0.08	Klhl33
ENSMUSG00000004939	110.2046302	-1.028345062	0.375539787	-2.7383119	0.006176	0.08	Nmrk2
ENSMUSG00000053044	133.6244505	-1.026533625	0.352252097	-2.9142016	0.003566	0.08	Cd8b1
ENSMUSG00000000823	133.6440201	-1.024737174	0.329352594	-3.1113682	0.001862	0.08	Zfp512b
ENSMUSG00000042743	564.528371	-1.018085868	0.390362563	-2.608052	0.009106	0.08	Sgtb
ENSMUSG00000051379	1706.04725	-1.017533722	0.40255492	-2.5276892	0.011482	0.08	Flrt3
ENSMUSG00000109704	198.7140702	-1.010516938	0.328638514	-3.0748585	0.002106	0.08	Gm38414
ENSMUSG00000078967	123.6378305	-1.009559591	0.409958578	-2.4625893	0.013794	0.08	Gapdh-ps16
ENSMUSG00000031922	3729.136003	-1.009403791	0.325752313	-3.098685	0.001944	0.08	Cep57
ENSMUSG00000097207	129.3001498	-1.009294516	0.36961708	-2.730649	0.006321	0.08	6030443J06Rik